bioRxiv preprint doi: https://doi.org/10.1101/152975; this version posted July 31, 2017. The copyright holder for this preprint (which was not certified by peer review) is the author/funder, who has granted bioRxiv a license to display the preprint in perpetuity. It is made available under aCC-BY 4.0 International license.

1
2
3
4
5 **Opposing spatial gradients of inhibition and neural activity in mouse olfactory cortex**

6 Adam M. Large, Nathan W. Vogler, Martha Canto-Bustos, Paul Schick and Anne-Marie M. Oswald

7 Department of Neuroscience, Center for the Neural Basis of Cognition,

8 University of Pittsburgh, Pittsburgh, PA, United States, 15213

9
10
11

12 **Corresponding Author**:
13 Anne-Marie M. Oswald
14 Assistant Professor
15 Department of Neuroscience
16 University of Pittsburgh
17 A210 Langley Hall
18 Pittsburgh, PA, 15260
19 amoswald@pitt.edu
20
21
22
23

bioRxiv preprint doi: https://doi.org/10.1101/152975; this version posted July 31, 2017. The copyright holder for this preprint (which was not certified by peer review) is the author/funder, who has granted bioRxiv a license to display the preprint in perpetuity. It is made available under aCC-BY 4.0 International license.

24 **Abstract**

25 The spatial representation of stimuli in primary sensory cortices is a convenient scaffold for elucidating
26 the circuit mechanisms underlying sensory processing. In contrast, the anterior piriform cortex (APC)
27 lacks topology for odor identity and appears homogenous in terms of afferent and intracortical
28 excitatory circuitry. Here, we show that an increasing rostral-caudal (RC) gradient of inhibition onto
29 pyramidal cells is commensurate with a decrease in active neurons along the RC axis following
30 exploration of a novel odor environment. This inhibitory gradient is supported by somatostatin
31 interneurons that provide an opposing, rostrally-biased, gradient of inhibition to interneurons.
32 Optogenetic or chemogenetic modulation of somatostatin cells neutralizes the inhibitory gradient onto
33 pyramidal cells. This suggests a novel circuit mechanism whereby opposing spatial gradients of
34 inhibition and disinhibition regulate neural activity along the RC-axis. These findings challenge our
35 current understanding of the spatial profiles of neural circuits and odor processing within APC.

36

37

38

bioRxiv preprint doi: https://doi.org/10.1101/152975; this version posted July 31, 2017. The copyright holder for this preprint (which was not certified by peer review) is the author/funder, who has granted bioRxiv a license to display the preprint in perpetuity. It is made available under aCC-BY 4.0 International license.

39 It is well established that the spatial organization of sensory information plays an important role
40 in neocortical sensory processing. The retinotopic, tonotopic and somatotopic maps established at the
41 periphery form the basis of stimulus representation in primary visual, auditory and somatosensory
42 cortices. This spatial organization is perhaps the oldest and best understood feature of sensory codes.
43 In the olfactory system, odor components are encoded by individual olfactory receptor neurons
44 (ORNs) that express a single receptor gene. All ORNs expressing the same receptor project axons to
45 ~2 target glomeruli in the olfactory bulb (OB) [1,2]. Within the OB, individual mitral/tufted (M/T) cells
46 extend apical dendrites to a single glomerulus [3] and respond selectively to glomerular activation [4,5].
47 This extreme connection specificity produces a discrete spatial organization of odor information within
48 the OB [6-9]. However, just one synapse away in the anterior piriform cortex (APC), any semblance of
49 spatial representation for odor identity is lost.
50 The piriform cortex is a trilaminar cortex that extends along the rostral-caudal (RC) axis of the
51 ventral rodent brain. The two main subdivisions, anterior (APC) and posterior (PPC) piriform cortex,
52 differ with respect to afferent and efferent projections [10-12] as well as functional roles in olfactory
53 processing [13-16]. However, despite the fact that each region comprises ~1-2 mm of the RC axis, odor
54 processing within APC or PPC is considered spatially homogenous. The APC is delineated by the
55 lateral olfactory tract (LOT) that delivers odor information directly from the OB. Single M/T cell axons
56 branch extensively along the LOT [17-19] resulting in diffuse pattern of afferent excitation. Likewise,
57 recurrent connections between principal neurons within APC extend over millimeter distances [20,21].
58 Consistent with this distributed excitatory architecture, there is no topography for odor identity in APC.
59 Neurons responsive to a single odor are distributed along the RC-axis of the APC [22-24] and nearby
60 neurons respond to different odors [24-27]. The absence of an “odortopic” map, suggests that, unlike
61 sensory neocortex, space is not a dimension for odor coding in APC.
62 Nonetheless, there is evidence that odor evoked responses vary along the rostral-caudal axis of
63 APC. For example, odor evoked activity at rostral sites is denser [22], has lower concentration thresholds
64 [28], and has earlier response times [24,29-31] versus caudal sites. Further, in contrast to excitation,
65 intracortical inhibition is asymmetric along the RC axis [32]. Finally, rostral APC projects more densely to

bioRxiv preprint doi: https://doi.org/10.1101/152975; this version posted July 31, 2017. The copyright holder for this preprint (which was not certified by peer review) is the author/funder, who has granted bioRxiv a license to display the preprint in perpetuity. It is made available under aCC-BY 4.0 International license.

66 the OB and orbitofrontal cortex (OFC) while caudal APC and PPC project to agranular insula (AI) [11,33-35].
67 Thus, contrary to preconceived notions, space may be a relevant feature of olfactory processing in
68 APC. However, a central challenge is elucidating the circuit mechanisms and functional roles of RC
69 spatial patterning in APC.

70 In this study, we use optogenetic [36] and chemogenetic tools [37] as well as targeted-
71 recombination in active populations (TRAP) [38] to investigate the circuitry underlying the spatial profiles
72 of inhibition and neural activity in APC. Specifically, we find that inhibition of pyramidal cells (PC)
73 increases on a millimeter scale from rostral to caudal APC. Our findings suggest a disinhibitory circuit
74 mechanism, mediated by somatostatin interneurons, underlies the RC patterning of inhibition. This
75 increasing gradient of inhibition is commensurate with a context dependent, RC decrease in the density
76 of active neurons during odor exposure. Moreover we show that spatial patterning of inhibition and
77 neural activity is laminar dependent. Altogether, our findings provide new insights to the RC spatial
78 patterns of inhibition and neural activity in APC and suggest space is a dimension of olfactory
79 processing in cortex.

80 **Results**

81 *Asymmetric inhibitory circuitry in APC*

82 Spatially asymmetric inhibition of pyramidal cells (PC) in APC [32] has been previously
83 demonstrated using glutamate uncaging. Specifically, light evoked uncaging at caudal stimulation sites
84 yielded stronger inhibition of PCs compared to rostral sites. These findings are seemingly at odds with
85 the spatial profiles of excitation [17-21] and odor-evoked responses [26,27] that do not vary with space. This
86 led us to question, “How and why do inhibitory spatial asymmetries exist in APC?”

87 Since previous un-caging methods could activate both excitatory and inhibitory neurons, we
88 investigated whether inhibitory circuits alone are sufficient to reproduce inhibitory asymmetries. Whole
89 cell recordings were made from L2 principal excitatory neurons, namely semilunar cells (SL) and
90 superficial PCs (sPC) as well as deep PCs (dPC) in L3. Recorded neurons were centrally located along
91 the RC axis in sagittal slices of APC. Interneurons were specifically activated using Channelrhodopsin

bioRxiv preprint doi: https://doi.org/10.1101/152975; this version posted July 31, 2017. The copyright holder for this preprint (which was not certified by peer review) is the author/funder, who has granted bioRxiv a license to display the preprint in perpetuity. It is made available under aCC-BY 4.0 International license.

92 (ChR2) expressed under the promoter for vesicular GABA transporter (VGAT). VGAT-ChR2
93 interneurons were stimulated using restricted spots (~70 μm diameter) of blue light in 4x5 grid
94 surrounding the recorded cell (schematic, **Figure 1A, D1** [39]). The inhibitory strength was quantified as
95 the area (pAs) under IPSC evoked at each stimulation site **(Figure 1B1,C1, D2)**. We have previously
96 reported the inhibitory strength by cell type and layer [39]. Here, we quantify the asymmetry in inhibitory
97 strength evoked at rostral versus caudal sites. An asymmetric bias index was calculated as the
98 difference in average inhibition at caudal versus rostral stimulation sites (I_C-I_R), divided by the sum of
99 the inhibition from both sides (I_C+I_R), (**Figure 1B2,C2,D3**). Thus, solely caudal inhibition produces a
100 bias value of +1 while -1 corresponds to rostral inhibition. Inhibition was not significantly asymmetric in
101 SL cells (bias: 0.08 ± 0.11, p: 0.49, n=13, **Figure 1B2**). However, sPCs (L2) and dPCs (L3) received
102 significant, caudally biased inhibition (sPC bias: 0.22 ± 0.08, p: 0.016, n=14, **Figure 1C2**; dPC bias:
103 0.19 ± 0.05; p: 0.0012, n=16, one sample t-test, **Figure 1D3**). Thus, inhibitory circuitry alone is
104 sufficient to reproduce asymmetric inhibition of PCs along the RC-axis. Since we have previously found
105 that inhibition of sPCs is significantly weaker than dPCs, and inhibition from L3 is stronger than L2 [39],
106 we focused the remainder of our experiments on L3 dPCs.

107 One interpretation of these findings is that caudally located dPCs receive stronger inhibition
108 than rostral dPCs. To investigate this possibility, we compared local inhibitory strength in dPC pairs
109 (n=19) separated by (100-1000 μm) distances along the ~1.5 mm RC-axis. On average, the caudal
110 neuron of the pair received significantly stronger inhibition (4.18 ± 0.90 pAs) than the rostral neuron
111 (2.60 ± 0.68 pAs, p: 0.002, paired t-test, **Figure 1E1**). Moreover, as the distance between the rostral
112 and caudal neuron increased, the difference in inhibitory strength increased (slope: 5.8 ± 2.1 pAs/mm,
113 p: 0.013, R^2: 0.32, **Figure 1E2**). Finally, across the population of dPCs, inhibitory strength increased
114 with soma location relative to the rostral start of the LOT in the sagittal slice (slope: 5.4 ± 1.3 pAs/mm,
115 p: 0.0003, n=27, R^2: 0.41, **Figure 1F**). These findings demonstrate an increasing gradient of inhibition
116 onto dPCs with a spatial scale that extends >1.0 mm of the RC axis of APC.

bioRxiv preprint doi: https://doi.org/10.1101/152975; this version posted July 31, 2017. The copyright holder for this preprint (which was not certified by peer review) is the author/funder, who has granted bioRxiv a license to display the preprint in perpetuity. It is made available under aCC-BY 4.0 International license.

117 To test if stronger caudal inhibition is a general feature of APC we investigated inhibition of L2
118 and L3 interneurons using grid stimulation of VGAT-ChR2 interneurons (**Figure 2A**). L2 interneurons
119 received weaker inhibition (3.42 ± 0.5 pA) than L3 interneurons (7.02 ± 0.92 pAs, p: 0.0043, ANOVA-
120 Tukey, **Figure 2B**). In addition, L2 interneurons did not receive significantly asymmetric inhibition (bias:
121 0.04 ± 0.07, p: 0.11, n=18, **Figure 2C1, 2**). L3 interneurons received comparable inhibition to dPCs
122 (8.63 ± 0.84, p: 0.239, ANOVA-Tukey, **Figure 2B**). However, L3 interneurons received stronger
123 inhibition from rostral rather than caudal sites (bias: -0.13 ± 0.05, p: 0.013, n=25, **Figure 2D1,2**) and
124 bias indices of L3 interneurons significantly differed from dPCs (p: 0.0001, t-test, **Figure 2E**). Thus,
125 dPCs and L3 interneurons have opposing spatial profiles of inhibition- dPCs receive stronger inhibition
126 from caudal sites versus rostral sites (I_C: 0.63 ± 0.034, I_R: 0.44 ± 0.042 p: 0.003, paired t-test) and L3
127 interneurons receive significantly more inhibition from rostral sites versus caudal (I_R: 0.54 ± 0.033, $I_{C:}$
128 0.42 ± 0.034 p: 0.008, paired t-test **Figure 2F**).

129 How do inhibitory circuits implement opposing RC inhibitory asymmetries and what is the
130 functional role of this opposition? A simple mechanism to increase inhibition is to increase the number
131 of interneurons. Since the majority (~85%) of PC-targeting interneurons in L3 express parvalbumin
132 (PV), somatostatin (SST) and/or calbindin (CB) [40], we investigated the RC distributions of these three
133 interneuron classes. SST cells were identified as tdTom(+) cells in SST-Ai14 mice (**Figure 3A,** n=7
134 mice) while PV and CB cells were identified using anti-CB (**Figure 3B**, n=6 mice) or anti-PV
135 immunochemistry (**Figure 3C,** n=6 mice). To quantify interneuron density, somas were counted in L3
136 along 1 to 1.5 mm (0.1 mm increments) of the RC axis (**Figure 3A1-C1**, ROIs dashed areas). As
137 previously shown [40], the average densities (cells/mm^2) of SST (235 ± 14) and CB cells (174 ± 27) were
138 greater than PV cells (109 ± 9.0, p: 0.0054, KW-test). To investigate RC patterning, densities for each
139 section were normalized to the most rostral section (~2.46 mm from Bregma [41]). For each animal,
140 normalized density versus RC distance was linearly fit to obtain the slope of the change in density per
141 mm^{-1} (**Figure 3A1-C2**, **Table 1**). Only SST-cell densities consistently varied along the RC axis (**Figure**
142 **3A1-4, Table 1**). In the majority of mice (n=5/7), linear fits of SST cell density had significantly negative

bioRxiv preprint doi: https://doi.org/10.1101/152975; this version posted July 31, 2017. The copyright holder for this preprint (which was not certified by peer review) is the author/funder, who has granted bioRxiv a license to display the preprint in perpetuity. It is made available under aCC-BY 4.0 International license.

143 slope values (mean slope: -0.20 ± 0.04, p: 0.002, MWU-test, **Figure 3A4**, **Table 1**), and the average
144 normalized density across all animals (red filled circles, **Figure 3A3**) also decreased (slope: -0.25 ±
145 0.03, p<0.0001). The RC distributions of CB cells were highly variable with individual mice showing
146 increases (n=2, i.e. **Figure 3B1,2**), decreases (n=1) or no change (n=3) along the RC axis. The
147 distribution of CB slopes did not differ from zero (0.13 ± 0.16, p: 0.37, MW-test, **Figure B4**) and the
148 average normalized density did not change with RC distance (slope: 0.11 ± 0.17, p: 0.55, **Figure 3B3**).
149 PV cell density appears to decrease along the RC axis. However, this was only significant in one PV
150 animal (filled black circle, **Figure 3C4, Table 1**) and the average normalized density across all animals
151 (-0.27 ± 0.10, p: 0.031, **Figure 3C3**). In the majority of mice (n=5/6), PV cell density did not significantly
152 vary with RC distance and the distribution of slopes did not differ from zero (-0.16 ± 0.08, p: 0.065, MW-
153 test, open circles, **Figure 3C4**). Altogether, these findings suggest it is unlikely that stronger caudal
154 inhibition of dPCs arises from a rostral-to-caudal increase in interneuron density in L3.

155 We have previously shown that SST-cells inhibit the majority of L3 interneurons in APC [42].
156 This suggests that the high rostral density of SST cells could underlie rostrally-biased inhibition of
157 interneurons. To test this, we selectively expressed ChR2 in SST-cells and repeated grid stimulation
158 while recording IPSCs in L3 interneurons and dPCs (**Figure 4A**). As predicted, SST-cells provided
159 rostrally-biased inhibition to the majority (73%) of L3 interneurons (bias: -0.11 ± 0.04, p: 0.02, n=22,
160 **Figure 4B1,2**). Bias values did not significantly differ between VGAT-ChR2 and SST-ChR2 animals (p:
161 0.69, unpaired t-test). Thus, activating solely SST-cells replicates the rostrally-biased inhibition (I_R: 0.58
162 ± 0.03 > I_C: 0.048 ± 0.03, p: 0.017, paired t-test, **Figure 4D**) of L3 interneurons seen in VGAT-ChR2
163 animals. Interestingly, the strength of SST-mediated inhibition onto L3 interneurons also did not
164 significantly differ (6.82 ± 1.4 pAs) from that in VGAT-ChR2 animals (7.02 ± 0.92 pAs, p: 0.91, unpaired
165 t-test). Although one should be cautious comparing between transgenic lines, one interpretation is that
166 SST cells are a major source of rostrally-biased inhibition onto L3 interneurons.

167 In dPCs, SST-ChR2 mediated inhibition was significantly weaker (4.77 ± 0.89 pAs) than
168 VGAT-ChR2 (8.63 ± 0.84 pAs, p: 0.003, unpaired t-test). This would be expected if SST-cells are only a

bioRxiv preprint doi: https://doi.org/10.1101/152975; this version posted July 31, 2017. The copyright holder for this preprint (which was not certified by peer review) is the author/funder, who has granted bioRxiv a license to display the preprint in perpetuity. It is made available under aCC-BY 4.0 International license.

169 subset of the interneurons that inhibit dPCs. SST-ChR2 cells provided rostrally-biased inhibition to
170 50% of dPCs (n=7/14, **Figure 4C1**) compared to only 2/16 in VGAT-ChR2 animals. Consequently, the
171 distribution of bias values was not coherently asymmetric and did not differ from zero (0.06 ± 0.08, p:
172 0.45, one sample t-test, n=14, **Figure 4C2**). Finally, in contrast to VGAT-ChR2 activation, SST-ChR2
173 inhibition did not differ between rostral and caudal sites (p: 0.50 paired t-test, **Figure 4D**). Thus,
174 activation of solely SST-cells increases rostrally-biased inhibition of many dPCs and ultimately
175 neutralizes inhibitory bias across the population. These findings are consistent with rostrally-biased
176 distributions of SST-cells and suggest that additional inhibitory circuits are required to produce
177 consistent, caudally biased inhibition of dPCs.

178 There are two ways to produce caudally biased inhibition of dPCs - 1) increase caudal
179 inhibition; or 2) decrease rostral inhibition. We have not found a mechanism to support increased
180 caudal inhibition. However, we have shown that SST-cells provide rostral inhibition to interneurons
181 (**Figure 4B**), which could decrease rostral inhibition of dPCs. To test this possibility, we bred triple
182 transgenic animals that express ChR2 in all interneurons but only SST-cells express the inhibitory
183 DREADD, hM4Di (abbreviated: VGAT-ChR2-SST-Di). In these mice, the DREADD agonist CNO (20
184 μM, bath) reduces SST-cell activity. We performed grid stimulation of L3 sites (**Figure 4E**) and
185 compared IPSC strength and RC bias in control conditions (green) versus CNO (black, **Figure 4F**).
186 Upon application of CNO, IPSC strength decreased consistent with a loss of direct, SST mediated
187 inhibition of dPCs (Control: 4.14 ± 0.70 pAs; CNO: 2.72 ± 0.40 pAs, p: 0.007, paired t-test, n=12). If
188 SST-cells influence caudal bias through rostral disinhibition, we expect a loss in SST-mediated
189 inhibition would shift bias to less caudal values. Surprisingly, the mean bias did not change significantly
190 in CNO (bias: +0.17 ± 0.08, n=12) compared to control (bias: +0.19 ± 0.06, 0.57, paired t-test).
191 However, the bias distribution was significantly asymmetric in control conditions (mean>0, p: 0.010, one
192 sample t-test), whereas in CNO, bias values were not significantly asymmetric (p: 0.051, one sample t-
193 test). This is because caudal bias both increased (n=4/12) and decreased (n=8/12) across the dPC
194 population with CNO application. In a small number of dPCs, increased caudal bias (n=4/12, Δ_{Bias}=

bioRxiv preprint doi: https://doi.org/10.1101/152975; this version posted July 31, 2017. The copyright holder for this preprint (which was not certified by peer review) is the author/funder, who has granted bioRxiv a license to display the preprint in perpetuity. It is made available under aCC-BY 4.0 International license.

195 $Bias_{CNO}$-$Bias_{Control}$ =+0.13 ± 0.04, gray bars **Figure 4G**) can be explained by a loss of direct, SST-
196 mediated inhibition at rostral sites. In contrast, the majority of dPCs (n=8/12) shifted toward less caudal
197 bias values with CNO (Δ_{Bias} -0.09 ± 0.03, black bars, **Figure 4G**). In these cells, CNO produced a
198 significantly greater reduction in inhibition at caudal sites (-35 ± 9%) versus rostral sites (-24 ± 7%,
199 $p<0.05$, WSR-test, n=8). This suggests that rostral interneurons are normally suppressed by SST-cells
200 in control conditions, but rebound during CNO application and neutralize bias. Thus, caudally biased
201 inhibition of dPCs could arise by rostral disinhibition of PCs through SST-to-interneuron microcircuits.

202 *Rostral-caudal spatial profiles of neural activity*

203 What role might RC patterning of inhibition play in regulating neural activity during olfactory
204 processing? Although odor responsive neurons are distributed in APC, few studies have addressed the
205 spatial patterns of neural activity along the full extent of the APC [22,24,28]. To investigate the RC
206 patterning of neural activity in APC, we used targeted recombination in active populations (TRAP) in
207 $FosCre^{ERT}$ mice [38]. These mice express a tamoxifen-dependent cre-recombinase under the promoter
208 for the activity dependent, immediate early gene *c-fos.* We used $FosCre^{ERT}$x Ai14 mice to express the
209 fluorescent protein, tdTomato in neurons activated in the presence hydroxytamoxifen (4-OHT), (**Figure**
210 **5A, Supplemental Figure 1**). We measured the spatial distribution of active neurons along the RC axis
211 of APC in three conditions: home cage with no odor (HC), home cage with novel odor (HCO), or
212 exploration of a novel environment with novel odor (NEO) (**Figure 5B1,2**). Briefly, HC (n=6) and HCO
213 (n=6) mice were given a single dose of 4-OHT and then returned to the home cage. HCO mice were
214 allowed to rest for 30 min then exposed to odor in the home cage for 30 min. NEO mice (n=6) were
215 given 4-OHT, rested for 30 min, and then explored a novel environment plus odor for 30 min before
216 being returned to the home cage. The novel environment was a divided arena with two cups of
217 bedding- one odorized, one blank- at the end of each arm (**Figure 5B2,** schematic far right). In a
218 subset of mice (n=4), location within the arena was monitored. NEO mice were highly active and
219 sampled both arms as well as the center (C) of the arena throughout exposure period (30 min, **Figure**
220 **5B3**). Mice spent nearly equivalent time per visit in the odorized (8.1 ± 3.5 s) and blank (9.8 ± 3.5 s)

bioRxiv preprint doi: https://doi.org/10.1101/152975; this version posted July 31, 2017. The copyright holder for this preprint (which was not certified by peer review) is the author/funder, who has granted bioRxiv a license to display the preprint in perpetuity. It is made available under aCC-BY 4.0 International license.

221 arms, but visited the blank arm (49 ± 33 visits) more frequently than the odorized arm (25 ± 14 visits).
222 The majority of HCO and NEO mice were exposed to isoamyl acetate. One cohort of mice (n=2 HCO,
223 n=1 NEO) was exposed to ethyl-butyrate. Results did not differ between odors and were grouped.
224 Following odor exposure, mice remained in their home cages, undisturbed, in the dark for 10-12 hours.
225 Mice were sacrificed 5 days later and tdTom(+) neurons were counted along ~1.5 mm of the RC axis.
226 Neural activity was quantified as the density (cells/mm^2) of tdTom(+) cells in laminar regions of interest
227 (L2, L3 ROIs, **Figure 5A**) located directly under the LOT. Densities were normalized to the most rostral
228 section for linear fits as described for interneuron densities (**Figure 3**). Summary data is presented in
229 **Figure 5** and **Table 2**; representative mice from each group and odor are shown in **Supplemental**
230 **Figure 1**.

231 We found laminar differences in both the average density and the RC spatial pattern of active
232 neurons with odor exposure. In L2, the average density of tdTom(+) neurons (in cells/mm^2) was
233 significantly greater in odor-exposed animals, NEO (243 ± 43) and HCO (199 ± 13), compared to HC
234 animals (113 ± 18, p: 0.013 KW-test, **Figure 5F1**). In L3, average density did not vary with condition
235 (HC: 52 ± 11; HCO: 68 ± 5, and NEO: 76 ± 15, p: 0.149 KW-test, **Figure 5F2**). In contrast, we found
236 RC spatial patterning of neural activity in L3 (**Figure 5D**) but not L2 (**Figure 5C**). The normalized
237 density of tdTom(+) neurons was plotted against RC distance for individual mice (open triangles) and
238 averaged across animals (solid triangles, **Figure 5C,D**). RC patterning was defined as significant non-
239 zero slope values from linear fits of RC densities in individual animals as well as across animals within
240 a group (**Table 2)**. In L2, the distributions of slope values did not significantly differ from zero (HC: 0.39
241 ± 0.27; HCO: -0.01 ± 0.10; NEO: -0.08 ± 0.07 mm^{-1}, p: 0.065 - 0.38, MWU-test, **Figure 5C, Table 2**) or
242 between conditions (p: 0.104 KW-test, **Figure 5E1**). However, in L3, there was significant RC
243 patterning of active neurons that further differed between HC, HCO and NEO conditions (**Figure 5D,**
244 **E2**). All NEO mice showed a significant decrease in the density of active neurons along the RC axis
245 (filled red triangles, slope distribution ≠ 0: -0.45 ± 0.05 mm^{-1}, **p: 0.005, MWU-test, **Figure 5E2, Table**
246 **2**). Further, the distribution of slope values was significantly more negative in NEO mice than HCO or

bioRxiv preprint doi: https://doi.org/10.1101/152975; this version posted July 31, 2017. The copyright holder for this preprint (which was not certified by peer review) is the author/funder, who has granted bioRxiv a license to display the preprint in perpetuity. It is made available under aCC-BY 4.0 International license.

247 HC (★★, p: 0.0046, KW-test, **Figure 5E2**). Consistent with findings from individual NEO animals, the
248 average change in RC density across animals was also significantly negative (red triangles, -0.47 ±
249 0.04, p<0.000, **Figure 5D3**). In HCO animals, RC patterning was shallower and less reliable in
250 individual mice than NEO animals. The average density across animals decreased significantly with RC
251 distance but the slope was less than half that of NEO animals (gold triangles: -0.19 ± 0.04; p: 0.0005,
252 linear regression, **Figure 5D2**). Further, although the distribution of slopes across mice was significantly
253 non-zero (-0.21 ± 0.12 mm^{-1}, **p: 0.005, MWU-test), RC decreases were rarely significant in individual
254 mice (n=2, filled orange triangles, **Figure 5E2, Table 2**). In HC animals, the average density across
255 animals appears to increase with RC distance (slope: 0.24 ± 0.10 mm^{-1}; p: 0.037, linear regression,
256 **Figure 5D1**). However, in individual animals, the distribution of slopes was inconsistent- positive (n=3),
257 negative (n=2) and neutral (n=1) (**Table 2**) and did not significantly differ from zero (slope: 0.13 ± 0.14
258 mm^{-1}, **Figure 5E2**). Finally, across conditions, changes tdTom(+) densities do not correlate with
259 changes in the total number of cells along the RC axis. In 6 mice, two from each group (NEO, HCO,
260 HC) we quantified the RC density of all cells (DAPI stain) in L2 and L3 **(Supplemental Figure 2**). Total
261 cells consistently increased along the RC axis in L2 (slope distribution ≠ 0: 0.54 ± 0.21 mm^{-1}, p: 0.0051
262 MWU) but not in L3 (0.08 ± 0.11 mm^{-1}, p: 0.94 MWU, n=6). To summarize, we show that odor exposure
263 increases the density of active neurons in L2 but not L3, and significantly changes the RC spatial
264 patterning of neural activity in L3 but not L2. The lack of consistent, significant RC patterning in
265 individual mice in HC and HCO animals, suggests that spatial patterning within APC is not a reliable
266 feature of odor processing in familiar environments. In contrast, exploration of a novel odor environment
267 (NEO) strongly and reliably changes RC spatial patterning in L3 compared to HCO, and HC contexts.
268 This suggests that space may be an avenue to differentially process odor information depending on
269 context.

270 In the first section of this study, we show that inhibition of dPCs in L3 increases along the
271 rostral-caudal axis on the spatial scale of millimeters. We find that a disinhibitory circuit mediated by
272 SST-cells supports this gradient through rostrally-biased inhibition of interneurons (**Figure 6A**). Could

bioRxiv preprint doi: https://doi.org/10.1101/152975; this version posted July 31, 2017. The copyright holder for this preprint (which was not certified by peer review) is the author/funder, who has granted bioRxiv a license to display the preprint in perpetuity. It is made available under aCC-BY 4.0 International license.

273 these RC asymmetries in inhibition play a role in the RC patterning of neural activity in L3 during odor
274 exposure? In NEO animals, neural activity in L3 decreases from rostral to caudal APC over a spatial
275 scale of millimeters (**Figure 5D2**) comparable to that of increasing inhibition in dPCs (**Figure 1F**). In
276 **Figure 6B,** we plot the average normalized decrease in active L3 neurons in NEO mice and the
277 average normalized increase in inhibition of dPCs along the RC axis. We find that the spatial scales of
278 neural activity and inhibition are well matched with opposing slopes (NEO: slope -0.47 ± 0.04 mm^{-1}, R:
279 0.94, p<0.0001; Inhibition: slope 0.67 ± 0.06 mm^{-1}, R: 0.98, p: 0.0001). Thus, when inhibition is
280 weakest, neural activity is maximal (rostral) and when inhibition is strongest, neural activity is minimal
281 (caudal). These findings suggest that inhibitory circuitry could underlie RC patterning of neural activity
282 in L3 of APC. Further, the recruitment of inhibitory gradients and may depend on the context of odor
283 experience. In contrast, inhibition is weaker in L2 where the spatial profiles of neural activity are
284 approximately uniform in L2 and do not seem to vary with odor context. Altogether, these laminar and
285 RC differences in inhibition and neural activity suggest spatially dependent and independent
286 mechanisms work in parallel during odor processing in APC.

287 **Discussion**

288 In this study, we demonstrate rostral-caudal spatial patterning in inhibitory circuitry and neural
289 activity in APC. Our findings reproduce earlier studies that have shown caudally-biased asymmetric
290 inhibition of PCs [32] and a RC decline in fos(+) neurons following odor exposure [22]. However, the
291 underlying circuitry and functional significance of these findings are unknown. Here, we provide three
292 major advances. First, we describe a disinhibitory circuit mediated by SST-cells that decreases rostral
293 inhibition relative to caudal inhibition in L3 PCs. Second, we show that RC patterning of neural activity
294 is confined to L3 and differs with odor exposure in familiar (HCO) versus novel (NEO) contexts. Finally,
295 the density of active neurons decreases along the RC axis following odor exposure in the NEO context
296 commensurate with increasing inhibition of L3 PCs. Specifically, rostral PCs are more active and
297 receive significantly less inhibition (disinhibited) whereas caudal PCs receive stronger inhibition and are

bioRxiv preprint doi: https://doi.org/10.1101/152975; this version posted July 31, 2017. The copyright holder for this preprint (which was not certified by peer review) is the author/funder, who has granted bioRxiv a license to display the preprint in perpetuity. It is made available under aCC-BY 4.0 International license.

298 less active. Altogether, our findings provide new evidence for RC spatial organization within APC as
299 well as a potential circuit mechanism for varying olfactory processing in different contexts.

300 *Disinhibition by Somatostatin Interneurons*

301 Inhibition plays a critical role in the processing and representation of sensory information in the cortex
302 [43]. In APC, inhibition balances excitation [39,44,45], narrows synaptic integration windows [20,44-48], supports
303 oscillatory activity and sharpens odor tuning [23,49-51]. Despite the prominent role inhibition plays in
304 shaping cortical responses, few studies have addressed circuits that modulate inhibition in APC [49,51]. In
305 neocortex, a number of disinhibitory circuits have been implicated in the gating or tuning of cortical
306 responses to sensory stimuli [52-59]. For example, SST-cells inhibit a range of interneuron classes
307 including fast-spiking, PV interneurons both in neocortex [56,57] and APC [42,51]. In this study, we show that
308 SST interneurons provide rostrally-biased inhibition to L3 interneuron and thus, mediate rostral
309 disinhibition of PCs. Disrupting this disinhibitory circuit through selective optogenetic activation or
310 chemogenetic inhibition of SST cells neutralizes the caudally-biased inhibitory gradient onto dPCs.
311 These findings suggest that SST-cells both inhibit [42] and disinhibit PCs in APC and play a role in the
312 RC patterning of inhibition.

313 Recent studies have shown that SST interneuron activity is modulated in different contexts. In
314 sensory neocortices, SST-cell activity is enhanced by cholinergic modulation [56,60,61], running during
315 visual sensory stimulation [62], or engagement in an auditory task [61]. In somatosensory cortex, whisking
316 specifically increases the firing rates of fast-spiking, SST-cells that preferentially inhibit PV cells [56,59].
317 Likewise, we have shown that two-thirds of SST cells in APC are FS and strongly inhibit PV-like cells [42].
318 Given that sniffing and whisking are correlated [63,64], an intriguing possibility is that actively exploring
319 (running, sniffing and whisking) a novel odor environment (NEO) globally enhances SST-cell activity in
320 sensory cortices. We propose that in APC, enhanced SST-cell activity gates rostral disinhibition and
321 increases in rostral neural activity in NEO animals. This interpretation is consistent with recent studies
322 that show interactions between interneurons in network models [65] promote context dependent changes
323 in network activity [58,61].

324 *Spatial patterning of neural activity in APC.*

bioRxiv preprint doi: https://doi.org/10.1101/152975; this version posted July 31, 2017. The copyright holder for this preprint (which was not certified by peer review) is the author/funder, who has granted bioRxiv a license to display the preprint in perpetuity. It is made available under aCC-BY 4.0 International license.

325 The spatial patterning is difficult to investigate *in vivo* due to the extent (~1.5 mm) and ventral location
326 of APC. Population imaging shows minimal spatial variation in response to different odors or intensities,
327 but typically only sample L2 neurons across ~300 μm of the RC axis [25-27]. Multi-site unit recordings
328 broadly sample the RC axis and suggest RC variation in odor-evoked firing rates [24] but sample a small
329 proportion of neurons per region. Likewise, intrinsic signal imaging or local field potential (LFP)
330 recordings broadly sample the RC axis and suggest systematic variation along the RC-axis in
331 concentration thresholds [28] and oscillatory activity respectively [13,29,30,66]. But these tools lack the fine
332 resolution to identify the neural circuits contributing to these responses.

333 To investigate the spatial profiles neural activity *in vivo*, we used TRAP-mice that conditionally
334 express of cre-recombinase linked to the IEG, *c-fos* [38]. This tool provides sufficient spatial scale to
335 investigate population activity along the entire RC axis at a resolution amenable microcircuit analysis.
336 TRAP-mice are advantageous over traditional IEG methods because cre-recombinase promotes
337 continuous cytoplasmic expression of tdTom independent of initial strength of activation. The limitation
338 is that the temporal window for capturing activity is longer. Labeling is optimal within one hour of 4-
339 OHT injection and declines significantly ~6 hours post injection [38,67]. Thus, neural densities are
340 expected to be higher in TRAP animals due to enhanced labeling of weak responses and potential
341 spurious labeling over long time windows. To minimize the latter, animals were undisturbed in the dark
342 for 10h following exposure and HC animals provided a baseline for handling and non-specific labeling.

343 Consistent with previous IEG immunolabeling [22,68,69], the density of activated, TRAP-tdTom(+)
344 cells increases significantly in odor-exposed animals (HCO and NEO) compared to HC animals. We
345 find these changes in density are restricted to L2 whereas RC patterning of neural activity occurs in L3.
346 A lack of RC patterning in L2 was initially surprising since L2 sPCs also receive caudally-biased
347 inhibition. However, L2 sPCs receive weaker inhibition than L3 dPCs [39] while L2 semilunar cells and
348 interneurons do not receive asymmetric inhibition. This suggests that the uniformly distributed spatial
349 pattern of neural activity in L2 is inherited from the spatial profile of afferent and/or recurrent excitation
350 [18-20]. In contrast, interneuron densities, particularly SST cells, are greatest in L3 [40,42]. We show that
351 individual L3 dPCs receive strong inhibition that increases with caudal position along the RC axis with

bioRxiv preprint doi: https://doi.org/10.1101/152975; this version posted July 31, 2017. The copyright holder for this preprint (which was not certified by peer review) is the author/funder, who has granted bioRxiv a license to display the preprint in perpetuity. It is made available under aCC-BY 4.0 International license.

352 the same spatial scale as decreases in neural activity. These are ideal conditions for inhibition to
353 dictate L3 RC activity patterns. Altogether, laminar differences in inhibition and RC patterning coincide
354 with layer-specific differences PC subclasses and projection targets [70,71] and support the premise that
355 parallel processing streams exist in APC.

356 *Functional roles for RC asymmetries in olfactory processing*

357 Given the seemingly uniform profile of excitation in APC, a surprising finding is that inhibitory
358 strength increases along the rostral-caudal axis. In entorhinal cortex, a dorsal-ventral inhibitory gradient
359 coincides with an increase in PV interneuron density, changes in receptive field size and increased
360 gamma oscillatory power [72]. We find SST cells rather than PV cells change in density along the RC
361 axis. Since SST-cell inhibition has a subtractive effect on PC odor tuning [51], it is possible that SST-
362 mediated inhibition of PCs supports changes in odor tuning across the RC extent of APC. Alternatively,
363 RC patterning of inhibition and neural activity could bias projections from rostral versus caudal APC in
364 different contexts. For example, higher rostral activity during NEO exploration could preferentially
365 increase feedback to the OB [73] or output to the OFC [11,33]. Finally, RC variation in inhibition may also
366 interact with other RC asymmetries to affect the spatial profiles of neural activity in APC. For example,
367 tufted cells afferents are limited to the rostral-ventral APC [18] and the overall density of OB afferents
368 decreases along the RC extent of the LOT. Likewise, projections from PPC [74] and frontal cortex [11,34]
369 also show RC biases. It remains to be determined if the various sources of RC asymmetry work in
370 concert during olfactory processing. Nonetheless, our study adds to a growing body of evidence that,
371 despite the lack of a topographic code for odor identity, space is a relevant dimension in olfactory
372 processing in piriform cortex.

373

374 **Methods**

375 *Animals:* A number of transgenic mouse lines and crosses were used in this study. VGAT-ChR2 mice
376 (*VGAT-Chr2:* B6.Cg-Tg(Slc32a1-COP4*H134R/EYFP)8Gfng/J) express channelrhodopsin in all

bioRxiv preprint doi: https://doi.org/10.1101/152975; this version posted July 31, 2017. The copyright holder for this preprint (which was not certified by peer review) is the author/funder, who has granted bioRxiv a license to display the preprint in perpetuity. It is made available under aCC-BY 4.0 International license.

377 interneurons [75]. The *SST-Cre* (B6:Sst<tm2.1(cre)Zjh>/J) mice were crossed with *Ai32 mice* (B6:129S-
378 Gt(ROSA)26Sortm32(CAG-COP4*H134R/EYFP)Hze/J) or DREADDi mice (B6N.129-
379 *Gt(ROSA)26Sortm1(CAG-CHRM4*,-mCitrine)Ute*/J) to express channelrhodopsin or the inhibitory
380 DREADD, hM4Di [37]. TRAP mice (FosCre^{ERT}: (B6.129(Cg)-Fos(tm1.1(cre/ERT2)Luo/J) were crossed
381 with Ai14 (B6.Cg-*Gt(ROSA)26Sortm14 (CAG-tdTomato)Hze*/J) to conditionally express tdtomato [38]. All
382 mice are from Jackson Laboratories. Mice were housed in groups of 2-5 animals on a 10:14 light/dark
383 cycle unless otherwise stated. All experiments involved mice of both sexes and age ranges from P20-
384 P300 as indicated.

385 *Slice preparation:* Brain slices of anterior piriform cortex (APC) were prepared from mice aged P19-35.
386 The mice were anesthetized with isoflurane and decapitated. The brain was removed from the skull
387 and immersed in ice cold oxygenated (95% O_2-5% CO_2) ACSF (in mM: 125 NaCl, 2.5 KCl, 25 $NaHCO_3$,
388 1.25 NaH_2PO_4, 1.0 $MgCl_2$, 25 Dextrose, 2.5 $CaCl_2$) (all chemicals from Sigma, USA unless otherwise
389 stated). Parasagittal slices (300 μm) were made using a vibratome (Leica Biosystems) in ice cold
390 ACSF. The slices were transferred to warm ACSF (37°C) for 30 min and then rested at 20-22°C for 1
391 hour prior to recording (31-35°C). All surgical procedures were approved by the University of Pittsburgh
392 IACUC.

393 *Electrophysiology*: Whole cell, voltage and current clamp recordings were performed using a
394 MultiClamp 700B amplifier (Molecular Devices, Union City, CA). Data were low pass filtered (4 kHz)
395 and digitized at 10 kHz using an ITC-18 (Instrutech) controlled by custom software (Recording Artist,
396 https://bitbucket.org/rgerkin/recording-artist) written in IgorPro (Wavemetrics). Recording pipettes (4-10
397 MΩ) were pulled from borosilicate glass (1.5 mm, outer diameter) on a Flaming/Brown micropipette
398 puller (Sutter Instruments). The series resistance (<20 MΩ) was not corrected. The intracellular
399 solution consisted of (in mM) 130 K-gluconate, 5 KCl, 2 $MgCl_2$, 4 ATP-Mg, 0.3 GTP, 10 HEPES, and 10
400 phosphocreatine, 0.05% biocytin, 4.5 μM QX-314. Recordings were obtained from L2/3 pyramidal cells
401 (PCs), L2 semilunar (SL) cells as well as interneurons in L2/3. Neurons were visualized using infrared-
402 differential interference contrast microscopy (IR-DIC, Olympus). In transgenic mice, interneurons were

bioRxiv preprint doi: https://doi.org/10.1101/152975; this version posted July 31, 2017. The copyright holder for this preprint (which was not certified by peer review) is the author/funder, who has granted bioRxiv a license to display the preprint in perpetuity. It is made available under aCC-BY 4.0 International license.

403 targeted using fluorescence (YFP) and PCs as the absence of fluorescence. For all neurons, intrinsic
404 subthreshold properties such as input resistance, and time constant were assessed using a series of
405 hyperpolarizing and depolarizing current steps (-50 pA to 50 pA, 1 s duration). Neural identity was
406 confirmed post hoc using intrinsic properties and anatomical analysis of biocytin fills.

407 *Light stimulation:* Blue light (λ=460-488 nm, GFP block, Olympus) for optical stimulation was provided
408 by metal halide lamp (200W, Prior Scientific) passed through the microscope objective (60x, immersion,
409 Olympus). Light pulses were controlled using a mechanical shutter (Sutter Instruments). The light spot
410 was restricted to a ~70 µm diameter (0.5 mW) using the minimum aperture. To obtain the spatial profile
411 of inhibition, interneurons were focally activated in a 5x4 grid pattern while IPSCs were recorded in
412 interneurons or PCs. The horizontal axis of the grid was centered on the recorded neuron with
413 stimulation sites ranging from -300 µm (rostral) to +300 µm (caudal) at 150 µm increments. The vertical
414 axis ranged L1 to L3 in 125 µm increments corresponding to different lamina. Each grid site was
415 stimulated with 2 light pulses (20 ms duration, 100 ms interpulse interval, 15 s between trials). The 20
416 ms duration was chosen to reliably evoke least one spike and rarely 2 spikes in response to a single
417 pulse of direct somatic stimulation using the 70 µ spot at 0.5 mW [39]. Grids were repeated 3-7 times per
418 neuron and each grid site was stimulated once every 6 min. Since solely inhibitory neurons are
419 activated and there is little evidence of depolarizing inhibition, polysynaptic responses are unlikely
420 under these recording conditions.

421 *CNO Application*: Stock solutions (10 mM in 0.9% saline) of the DREADD agonist, Clozapine-N-oxide
422 (CNO), were made fresh for each cohort of animals, aliquoted and stored at -20°C for up to 2 weeks.
423 On the day of experiment, CNO stock was diluted (20 µM in ACSF) for bath application.

424 *Analysis of inhibition:* Electrophysiology traces of IPSCs are presented as the average across trials
425 (n=3-7) for individual neurons. IPSC strength was taken as the area (pAs) under the first IPSC of the
426 pair of light pulses. The second IPSC was not analyzed due to unreliable AP firing on the second light
427 pulse [39]. Average PSCs with minimum amplitude of 10 pA were included for analyses; smaller PSCs
428 were not distinguishable from noise and given a value of 0. To compare the spatial profiles of inhibition

bioRxiv preprint doi: https://doi.org/10.1101/152975; this version posted July 31, 2017. The copyright holder for this preprint (which was not certified by peer review) is the author/funder, who has granted bioRxiv a license to display the preprint in perpetuity. It is made available under aCC-BY 4.0 International license.

429 across animals IPSC amplitudes were normalized to the strength of the maximum IPSC regardless of
430 location in the grid. The rostral-caudal bias was taken as the average normalized inhibition from the
431 caudal sites minus the average inhibition of the rostral sites, divided by the summed inhibition from both
432 sides. The bias metric ranges from -1 (rostral bias) to +1 (caudal bias). Since L1 inhibition was typically
433 weak [39] these sites were excluded from the bias metric.

434 *TRAP-mice:* To label active neurons during odor exposure, we used TRAP mice. Briefly, $FosCre^{ERT}$
435 mice express a tamoxifen-dependent cre-recombinase under the promoter for the activity dependent,
436 immediate early gene *c-fos*. $FosCre^{ERT}$ mice were crossed with Ai14 mice and the offspring
437 conditionally express tdTomato (tdTom) in active neurons upon tamoxifen administration. We used 4-
438 hydroxytamoxifen (4-OHT) (Sigma) because the time window of activation was faster and narrower
439 than tamoxifen [38]. Doses of 4-OHT were freshly made on the day of injection. Briefly, 4-OHT (15 mg)
440 was dissolved in in 100% ethanol (200µl) by sonication at 37°C (~1 hr). Then peanut oil (1.5 ml, Sigma)
441 was added and ethanol was removed via centrifugation (15 min) and vacuum evaporation (1-2 hrs).
442 The final solution (50mg/kg) was filtered (0.2 µm) and administered by intraperitoneal injection (~150-
443 200 µl per animal) 30 min before odor exposure.

444 *Odor exposure and behavior:* There were three groups of TRAP-mice (P90-300): 1) home cage
445 animals (HC), 2) home cage plus odor (HCO), and 3) novel environment plus odor (NEO). Experiments
446 were done serially, with 3-4 mice per cohort. In each cohort, there was typically at least one mouse per
447 condition. However, there were losses due to death (n=2), poor perfusion (n=2) and insufficient 4-OHT
448 dosage (n=3). Whenever possible, mice from the same litter were used for each cohort or nearly age-
449 matched litters (± 1 week) were used. Mice were singly housed on a 12:12 light/dark cycle and all
450 testing was done ±1 hr from the onset of the dark cycle. Mice were food restricted (90% body weight)
451 as well as handled and weighed daily for 3 days prior to 4-OHT injection and odor exposure. Odor
452 stimuli were isoamyl acetate (Sigma) or ethyl butyrate (Sigma) at 1:100 dilution in mineral oil. For HCO
453 animals, 100 µl of odor was applied to a cotton ball in an open tube that was placed in the cage for 30
454 min. For NEO mice, filter paper (0.5 x 0.5 cm) was saturated with odor and then buried in a paper cup

bioRxiv preprint doi: https://doi.org/10.1101/152975; this version posted July 31, 2017. The copyright holder for this preprint (which was not certified by peer review) is the author/funder, who has granted bioRxiv a license to display the preprint in perpetuity. It is made available under aCC-BY 4.0 International license.

455 filled with clean bedding. To encourage exploration, the cup of odorized bedding was placed at the end
456 of one arm of a divided arena (20 x 10 inches) and a blank cup of bedding in the other arm (**Figure**
457 **5B2)**. Following 4-OHT administration and exposure, animals were returned to their home cages and
458 undisturbed in the dark for 10-12 hours. Mice were sacrificed 5 days post 4-OHT and neural activity in
459 each context was quantified as the density of tagged, tdTom(+) neurons in L2 and L3 of APC. The
460 average densities of tdTom cells across L2/3 ranged from ~70-400 cells/mm^2 depending on condition.
461 A minimum average density of 30 cells/mm^2 was set as a lower threshold for inclusion of an animal in
462 the data set. In three excluded animals, densities were <10 cells/mm^2 suggesting that 4-OHT dosage
463 was insufficient.

464 *Anatomy*: Mice were given an overdose of ketamine-xylazine. Mice were then perfused transcardially
465 (20 ml/min) with 0.1 M sodium phosphate buffer (PB), followed by 200 ml of 4% paraformaldehyde
466 (PFA) in 0.2M PB. Brains were removed and fixed in 4% PFA overnight at 4°C, then transferred to a
467 sucrose solution. Coronal slices (50 µm) were cut using a freezing microtome maintained in phosphate
468 buffer prior to immunochemistry (anti-PV or anti-CB staining) and/or mounting. Parvalbumin (PV) cells
469 were immunostained using rabbit anti-parvalbumin (PV27, Swant, 1:1000). Calbindin cells were
470 immunostained using rabbit anti-calbindin D-28K (CB38, Swant, 1:1000). In both cases, the secondary
471 was donkey anti-rabbit Alexa-fluor-488 (#A21206 Life Technologies, 1:500). Every other section was
472 mounted using fluoromount to protect fluorescence and minimize background. Sections were imaged
473 on a Nikon Eclipse-Ci microscope at 4x magnification. Illumination was provided by a mercury lamp
474 (Nikon Intensilight) and delivered through appropriate filter blocks for GFP (495 nm) and tdTomato (585
475 nm). Light intensity and exposure duration (100-400 ms) were optimized for the first section in a series
476 using automated software (Nikon Elements), then maintained for ensuing sections. Sections were
477 photographed using a CCD HD color camera (Nikon DsFi2).

478 *Cell counts*: Neural densities were quantified as number of cells per mm^2 in laminar regions of interest
479 (ROI) located directly under the lateral olfactory tract in APC. Counts were made in a single focus plane
480 (4x magnification) for each section chosen to maximize the number of cells in focus. Automated counts

bioRxiv preprint doi: https://doi.org/10.1101/152975; this version posted July 31, 2017. The copyright holder for this preprint (which was not certified by peer review) is the author/funder, who has granted bioRxiv a license to display the preprint in perpetuity. It is made available under aCC-BY 4.0 International license.

481 of somas were obtained based on fluorescence intensity and circularity using Elements Software
482 (Nikon). Two researchers independently verified all counts with at least one blind to condition. In the
483 event of discrepancy, a third individual, blind to condition, performed counts. Every other coronal
484 section (8-15 sections per animal) was analyzed spanning 1-1.5 mm along the rostral-caudal extent of
485 the APC. The average density was taken across all sections in a given animal. To assess rostral-
486 caudal spatial patterning, densities in each section were normalized to the most rostral section
487 corresponding to ~2.46 mm from Bregma [41]. For each animal, the slope of the least-squares linear
488 regression between normalized density and RC distance was used to quantify spatial patterning.

489 *Statistics:* All data is presented as mean ± SE unless otherwise stated. Initial sample sizes were
490 determined based on previous studies [22, 57] using comparable techniques and statistical comparisons.
491 Power analyses were conducted following statistical analysis to ensure sufficient power (Supplemental
492 Tables 1,2,3). Statistical tests were performed using two tailed, one or two-sample, paired or unpaired
493 Student's t-test as appropriate. In cases of small sample sizes (<10) non-parametric tests were used,
494 including the Mann-Whitney U-test (MWU) for unpaired data and the Wilcoxon Signed Ranks test
495 (WSR) for paired data. For multiple comparisons we used ANOVA with post hoc Tukey Test (ANOVA-
496 Tukey). For groups with small sample sizes multiple comparisons were made using non-parametric,
497 Kruskal-Wallis tests (KW-test). All statistical tests are indicated in the main text and/or figure legends.

498 **Acknowledgements:** We thank Brent Doiron and Nathan Urban for helpful comments on this study
499 and manuscript. We thank Samantha Mielo for technical support. This work was supported by a
500 National Institute on Deafness and Other Communication Disorders Grant (R01 DC015139) to AMMO
501 and an RK Mellon Fellowship to AML.
502
503 **Author Contributions:** AML and AMMO designed the project, collected and analyzed
504 electrophysiological and anatomical data, and wrote the manuscript. NWV collected and analyzed
505 electrophysiological data. MCB, and PS collected and analyzed anatomical data.

506

507

bioRxiv preprint doi: https://doi.org/10.1101/152975; this version posted July 31, 2017. The copyright holder for this preprint (which was not certified by peer review) is the author/funder, who has granted bioRxiv a license to display the preprint in perpetuity. It is made available under aCC-BY 4.0 International license.

508 **References**

509 1. Mombaerts, P., Wang, F., Dulac, C., Chao, S.K., Nemes, A., Mendelsohn, M., Edmondson, J. & Axel, R.
510 Visualizing an olfactory sensory map. *Cell* **87**, 675-86 (1996).
511 2. Mori, K. & Sakano, H. How is the olfactory map formed and interpreted in the mammalian brain? *Annu*
512 *Rev Neurosci* **34**, 467-99 (2011).
513 3. Buonviso, N., Chaput, M.A. & Scott, J.W. Mitral cell-to-glomerulus connectivity: an HRP study of the
514 orientation of mitral cell apical dendrites. *J Comp Neurol* **307**, 57-64 (1991).
515 4. Davison, I.G. & Ehlers, M.D. Neural circuit mechanisms for pattern detection and feature combination in
516 olfactory cortex. *Neuron* **70**, 82-94 (2011).
517 5. Davison, I.G. & Katz, L.C. Sparse and selective odor coding by mitral/tufted neurons in the main olfactory
518 bulb. *J Neurosci* **27**, 2091-101 (2007).
519 6. Fried, H.U., Fuss, S.H. & Korsching, S.I. Selective imaging of presynaptic activity in the mouse olfactory
520 bulb shows concentration and structure dependence of odor responses in identified glomeruli. *Proc Natl*
521 *Acad Sci U S A* **99**, 3222-7 (2002).
522 7. Soucy, E.R., Albeanu, D.F., Fantana, A.L., Murthy, V.N. & Meister, M. Precision and diversity in an odor
523 map on the olfactory bulb. *Nat Neurosci* **12**, 210-20 (2009).
524 8. Spors, H., Wachowiak, M., Cohen, L.B. & Friedrich, R.W. Temporal dynamics and latency patterns of
525 receptor neuron input to the olfactory bulb. *J Neurosci* **26**, 1247-59 (2006).
526 9. Willhite, D.C., Nguyen, K.T., Masurkar, A.V., Greer, C.A., Shepherd, G.M. & Chen, W.R. Viral tracing
527 identifies distributed columnar organization in the olfactory bulb. *Proc Natl Acad Sci U S A* **103**, 12592-7
528 (2006).
529 10. Haberly, L.B. & Price, J.L. Association and commissural fiber systems of the olfactory cortex of the rat. *J*
530 *Comp Neurol* **178**, 711-40 (1978).
531 11. Illig, K.R. Projections from orbitofrontal cortex to anterior piriform cortex in the rat suggest a role in
532 olfactory information processing. *J Comp Neurol* **488**, 224-31 (2005).
533 12. Majak, K., Ronkko, S., Kemppainen, S. & Pitkanen, A. Projections from the amygdaloid complex to the
534 piriform cortex: A PHA-L study in the rat. *J Comp Neurol* **476**, 414-28 (2004).
535 13. Chabaud, P., Ravel, N., Wilson, D.A. & Gervais, R. Functional coupling in rat central olfactory pathways: a
536 coherence analysis. *Neurosci Lett* **276**, 17-20 (1999).
537 14. Gottfried, J.A., Winston, J.S. & Dolan, R.J. Dissociable codes of odor quality and odorant structure in
538 human piriform cortex. *Neuron* **49**, 467-79 (2006).
539 15. Kadohisa, M. & Wilson, D.A. Separate encoding of identity and similarity of complex familiar odors in
540 piriform cortex. *Proc Natl Acad Sci U S A* **103**, 15206-11 (2006).
541 16. Litaudon, P., Amat, C., Bertrand, B., Vigouroux, M. & Buonviso, N. Piriform cortex functional
542 heterogeneity revealed by cellular responses to odours. *Eur J Neurosci* **17**, 2457-61 (2003).
543 17. Ghosh, S., Larson, S.D., Hefzi, H., Marnoy, Z., Cutforth, T., Dokka, K. & Baldwin, K.K. Sensory maps in the
544 olfactory cortex defined by long-range viral tracing of single neurons. *Nature* **472**, 217-20 (2011).
545 18. Igarashi, K.M., Ieki, N., An, M., Yamaguchi, Y., Nagayama, S., Kobayakawa, K., Kobayakawa, R., Tanifuji,
546 M., Sakano, H., Chen, W.R. & Mori, K. Parallel mitral and tufted cell pathways route distinct odor
547 information to different targets in the olfactory cortex. *J Neurosci* **32**, 7970-85 (2012).
548 19. Sosulski, D.L., Bloom, M.L., Cutforth, T., Axel, R. & Datta, S.R. Distinct representations of olfactory
549 information in different cortical centres. *Nature* **472**, 213-6 (2011).
550 20. Franks, K.M., Russo, M.J., Sosulski, D.L., Mulligan, A.A., Siegelbaum, S.A. & Axel, R. Recurrent circuitry
551 dynamically shapes the activation of piriform cortex. *Neuron* **72**, 49-56 (2011).
552 21. Yang, J., Litscher, G., Sun, Z., Tang, Q., Kishi, K., Oda, S., Takayanagi, M., Sheng, Z., Liu, Y., Guo, W.,
553 Zhang, T., Wang, L., Gaischek, I., Litscher, D., Lippe, I.T. & Kuroda, M. Quantitative analysis of axon
554 collaterals of single pyramidal cells of the anterior piriform cortex of the guinea pig. *BMC Neurosci* **18**, 25
555 (2017).

bioRxiv preprint doi: https://doi.org/10.1101/152975; this version posted July 31, 2017. The copyright holder for this preprint (which was not certified by peer review) is the author/funder, who has granted bioRxiv a license to display the preprint in perpetuity. It is made available under aCC-BY 4.0 International license.

556 22. Illig, K.R. & Haberly, L.B. Odor-evoked activity is spatially distributed in piriform cortex. *J Comp Neurol*
557 **457**, 361-73 (2003).
558 23. Poo, C. & Isaacson, J.S. Odor representations in olfactory cortex: "sparse" coding, global inhibition, and
559 oscillations. *Neuron* **62**, 850-61 (2009).
560 24. Rennaker, R.L., Chen, C.F., Ruyle, A.M., Sloan, A.M. & Wilson, D.A. Spatial and temporal distribution of
561 odorant-evoked activity in the piriform cortex. *J Neurosci* **27**, 1534-42 (2007).
562 25. Roland, B., Deneux, T., Franks, K.M., Bathellier, B. & Fleischmann, A. Odor identity coding by distributed
563 ensembles of neurons in the mouse olfactory cortex. *Elife* **6**(2017).
564 26. Stettler, D.D. & Axel, R. Representations of odor in the piriform cortex. *Neuron* **63**, 854-64 (2009).
565 27. Tantirigama, M.L., Huang, H.H. & Bekkers, J.M. Spontaneous activity in the piriform cortex extends the
566 dynamic range of cortical odor coding. *Proc Natl Acad Sci U S A* **114**, 2407-2412 (2017).
567 28. Sugai, T., Miyazawa, T., Fukuda, M., Yoshimura, H. & Onoda, N. Odor-concentration coding in the
568 guinea-pig piriform cortex. *Neuroscience* **130**, 769-81 (2005).
569 29. Freeman, W.J. Distribution in time and space of prepyriform electrical activity. *J Neurophysiol* **22**, 644-65
570 (1959).
571 30. Litaudon, P. & Cattarelli, M. Piriform cortex late activity revealed functional spatial heterogeneity.
572 *Neuroreport* **6**, 1377-80 (1995).
573 31. Litaudon, P., Datiche, F. & Cattarelli, M. Optical recording of the rat piriform cortex activity. *Prog*
574 *Neurobiol* **52**, 485-510 (1997).
575 32. Luna, V.M. & Pettit, D.L. Asymmetric rostro-caudal inhibition in the primary olfactory cortex. *Nat*
576 *Neurosci* **13**, 533-5 (2010).
577 33. Chen, C.F., Zou, D.J., Altomare, C.G., Xu, L., Greer, C.A. & Firestein, S.J. Nonsensory target-dependent
578 organization of piriform cortex. *Proc Natl Acad Sci U S A* **111**, 16931-6 (2014).
579 34. Datiche, F. & Cattarelli, M. Reciprocal and topographic connections between the piriform and prefrontal
580 cortices in the rat: a tracing study using the B subunit of the cholera toxin. *Brain Res Bull* **41**, 391-8
581 (1996).
582 35. Ekstrand, J.J., Domroese, M.E., Johnson, D.M., Feig, S.L., Knodel, S.M., Behan, M. & Haberly, L.B. A new
583 subdivision of anterior piriform cortex and associated deep nucleus with novel features of interest for
584 olfaction and epilepsy. *J Comp Neurol* **434**, 289-307 (2001).
585 36. Boyden, E.S., Zhang, F., Bamberg, E., Nagel, G. & Deisseroth, K. Millisecond-timescale, genetically
586 targeted optical control of neural activity. *Nat Neurosci* **8**, 1263-8 (2005).
587 37. Zhu, H. & Roth, B.L. DREADD: a chemogenetic GPCR signaling platform. *Int J Neuropsychopharmacol*
588 **18**(2014).
589 38. Guenthner, C.J., Miyamichi, K., Yang, H.H., Heller, H.C. & Luo, L. Permanent genetic access to transiently
590 active neurons via TRAP: targeted recombination in active populations. *Neuron* **78**, 773-84 (2013).
591 39. Large, A.M., Vogler, N.W., Mielo, S. & Oswald, A.M. Balanced feedforward inhibition and dominant
592 recurrent inhibition in olfactory cortex. *Proc Natl Acad Sci U S A* **113**, 2276-81 (2016).
593 40. Suzuki, N. & Bekkers, J.M. Inhibitory neurons in the anterior piriform cortex of the mouse: classification
594 using molecular markers. *J Comp Neurol* **518**, 1670-87 (2010b).
595 41. Franklin, K. & Paxinos, G. *The Mouse Brain in Stereotaxic Coordinates* (Academic Press, 2007).
596 42. Large, A.M., Kunz, N.A., Mielo, S.L. & Oswald, A.M. Inhibition by Somatostatin Interneurons in Olfactory
597 Cortex. *Front Neural Circuits* **10**, 62 (2016).
598 43. Isaacson, J.S. & Scanziani, M. How inhibition shapes cortical activity. *Neuron* **72**, 231-43 (2011).
599 44. Sheridan, D.C., Hughes, A.R., Erdelyi, F., Szabo, G., Hentges, S.T. & Schoppa, N.E. Matching of feedback
600 inhibition with excitation ensures fidelity of information flow in the anterior piriform cortex.
601 *Neuroscience* **275**, 519-30 (2014).
602 45. Suzuki, N. & Bekkers, J.M. Distinctive classes of GABAergic interneurons provide layer-specific phasic
603 inhibition in the anterior piriform cortex. *Cereb Cortex* **20**, 2971-84 (2010a).
604 46. Luna, V.M. & Schoppa, N.E. GABAergic circuits control input-spike coupling in the piriform cortex. *J*
605 *Neurosci* **28**, 8851-9 (2008).

bioRxiv preprint doi: https://doi.org/10.1101/152975; this version posted July 31, 2017. The copyright holder for this preprint (which was not certified by peer review) is the author/funder, who has granted bioRxiv a license to display the preprint in perpetuity. It is made available under aCC-BY 4.0 International license.

606 47. Stokes, C.C. & Isaacson, J.S. From dendrite to soma: dynamic routing of inhibition by complementary
607 interneuron microcircuits in olfactory cortex. *Neuron* **67**, 452-65 (2010).
608 48. Suzuki, N. & Bekkers, J.M. Microcircuits mediating feedforward and feedback synaptic inhibition in the
609 piriform cortex. *J Neurosci* **32**, 919-31 (2012).
610 49. Birjandian, Z., Narla, C. & Poulter, M.O. Gain control of gamma frequency activation by a novel feed
611 forward disinhibitory loop: implications for normal and epileptic neural activity. *Front Neural Circuits* **7**,
612 183 (2013).
613 50. Poo, C. & Isaacson, J.S. A major role for intracortical circuits in the strength and tuning of odor-evoked
614 excitation in olfactory cortex. *Neuron* **72**, 41-8 (2011).
615 51. Sturgill, J.F. & Isaacson, J.S. Somatostatin cells regulate sensory response fidelity via subtractive
616 inhibition in olfactory cortex. *Nat Neurosci* **18**, 531-5 (2015).
617 52. Fu, Y., Kaneko, M., Tang, Y., Alvarez-Buylla, A. & Stryker, M.P. A cortical disinhibitory circuit for
618 enhancing adult plasticity. *Elife* **4**, e05558 (2015).
619 53. Fu, Y., Tucciarone, J.M., Espinosa, J.S., Sheng, N., Darcy, D.P., Nicoll, R.A., Huang, Z.J. & Stryker, M.P. A
620 cortical circuit for gain control by behavioral state. *Cell* **156**, 1139-52 (2014).
621 54. Lee, S., Kruglikov, I., Huang, Z.J., Fishell, G. & Rudy, B. A disinhibitory circuit mediates motor integration
622 in the somatosensory cortex. *Nat Neurosci* **16**, 1662-1670 (2013).
623 55. Letzkus, J.J., Wolff, S.B., Meyer, E.M., Tovote, P., Courtin, J., Herry, C. & Luthi, A. A disinhibitory
624 microcircuit for associative fear learning in the auditory cortex. *Nature* **480**, 331-5 (2011).
625 56. Munoz, W., Tremblay, R., Levenstein, D. & Rudy, B. Layer-specific modulation of neocortical dendritic
626 inhibition during active wakefulness. *Science* **355**, 954-959 (2017).
627 57. Pfeffer, C.K., Xue, M., He, M., Huang, Z.J. & Scanziani, M. Inhibition of inhibition in visual cortex: the logic
628 of connections between molecularly distinct interneurons. *Nat Neurosci* **16**, 1068-76 (2013).
629 58. Pi, H.J., Hangya, B., Kvitsiani, D., Sanders, J.I., Huang, Z.J. & Kepecs, A. Cortical interneurons that
630 specialize in disinhibitory control. *Nature* **503**, 521-4 (2013).
631 59. Xu, H., Jeong, H.Y., Tremblay, R. & Rudy, B. Neocortical somatostatin-expressing GABAergic interneurons
632 disinhibit the thalamorecipient layer 4. *Neuron* **77**, 155-67 (2013).
633 60. Chen, N., Sugihara, H. & Sur, M. An acetylcholine-activated microcircuit drives temporal dynamics of
634 cortical activity. *Nat Neurosci* **18**, 892-902 (2015).
635 61. Kuchibhotla, K.V., Gill, J.V., Lindsay, G.W., Papadoyannis, E.S., Field, R.E., Sten, T.A., Miller, K.D. &
636 Froemke, R.C. Parallel processing by cortical inhibition enables context-dependent behavior. *Nat*
637 *Neurosci* **20**, 62-71 (2017).
638 62. Pakan, J.M., Lowe, S.C., Dylda, E., Keemink, S.W., Currie, S.P., Coutts, C.A. & Rochefort, N.L. Behavioral-
639 state modulation of inhibition is context-dependent and cell type specific in mouse visual cortex. *Elife*
640 **5**(2016).
641 63. Deschenes, M., Kurnikova, A., Elbaz, M. & Kleinfeld, D. Circuits in the Ventral Medulla That Phase-Lock
642 Motoneurons for Coordinated Sniffing and Whisking. *Neural Plast* **2016**, 7493048 (2016).
643 64. Kurnikova, A., Moore, J.D., Liao, S.M., Deschenes, M. & Kleinfeld, D. Coordination of Orofacial Motor
644 Actions into Exploratory Behavior by Rat. *Curr Biol* **27**, 688-696 (2017).
645 65. Litwin-Kumar, A., Rosenbaum, R. & Doiron, B. Inhibitory stabilization and visual coding in cortical circuits
646 with multiple interneuron subtypes. *J Neurophysiol* **115**, 1399-409 (2016).
647 66. Litaudon, P. & Cattarelli, M. Multi-site optical recording of the rat piriform cortex activity. *Neuroreport* **5**,
648 743-6 (1994).
649 67. Cazzulino, A.S., Martinez, R., Tomm, N.K. & Denny, C.A. Improved specificity of hippocampal memory
650 trace labeling. *Hippocampus* **26**, 752-62 (2016).
651 68. Datiche, F., Roullet, F. & Cattarelli, M. Expression of Fos in the piriform cortex after acquisition of
652 olfactory learning: an immunohistochemical study in the rat. *Brain Res Bull* **55**, 95-9 (2001).
653 69. Roullet, F., Datiche, F., Lienard, F. & Cattarelli, M. Learning-stage dependent Fos expression in the rat
654 brain during acquisition of an olfactory discrimination task. *Behav Brain Res* **157**, 127-37 (2005).

bioRxiv preprint doi: https://doi.org/10.1101/152975; this version posted July 31, 2017. The copyright holder for this preprint (which was not certified by peer review) is the author/funder, who has granted bioRxiv a license to display the preprint in perpetuity. It is made available under aCC-BY 4.0 International license.

655 70. Brunjes, P.C. & Osterberg, S.K. Developmental Markers Expressed in Neocortical Layers Are Differentially
656 Exhibited in Olfactory Cortex. *PLoS One* **10**, e0138541 (2015).
657 71. Diodato, A., Ruinart de Brimont, M., Yim, Y.S., Derian, N., Perrin, S., Pouch, J., Klatzmann, D., Garel, S.,
658 Choi, G.B. & Fleischmann, A. Molecular signatures of neural connectivity in the olfactory cortex. *Nat*
659 *Commun* **7**, 12238 (2016).
660 72. Beed, P., Gundlfinger, A., Schneiderbauer, S., Song, J., Bohm, C., Burgalossi, A., Brecht, M., Vida, I. &
661 Schmitz, D. Inhibitory gradient along the dorsoventral axis in the medial entorhinal cortex. *Neuron* **79**,
662 1197-207 (2013).
663 73. Padmanabhan, K., Osakada, F., Tarabrina, A., Kizer, E., Callaway, E.M., Gage, F.H. & Sejnowski, T.J.
664 Diverse Representations of Olfactory Information in Centrifugal Feedback Projections. *J Neurosci* **36**,
665 7535-45 (2016).
666 74. Haberly, L.B. & Price, J.L. Association and commissural fiber systems of the olfactory cortex of the rat. II.
667 Systems originating in the olfactory peduncle. *J Comp Neurol* **181**, 781-807 (1978).
668 75. Zhao, S., Ting, J.T., Atallah, H.E., Qiu, L., Tan, J., Gloss, B., Augustine, G.J., Deisseroth, K., Luo, M.,
669 Graybiel, A.M. & Feng, G. Cell type-specific channelrhodopsin-2 transgenic mice for optogenetic
670 dissection of neural circuitry function. *Nat Methods* **8**, 745-52 (2011).

671
672
673
674
675
676
677
678
679
680
681
682
683
684
685

bioRxiv preprint doi: https://doi.org/10.1101/152975; this version posted July 31, 2017. The copyright holder for this preprint (which was not certified by peer review) is the author/funder, who has granted bioRxiv a license to display the preprint in perpetuity. It is made available under aCC-BY 4.0 International license.

686

	SST			PV			CB		
Mouse	Slope	R^2	P	Slope	R^2	P	Slope	R^2	P
1	**-0.13 ± 0.03**	**0.48**	**0.0014**	-0.07 ± 0.20	0.02	0.7385	0.08 ± 0.09	0.06	0.3827
2	**-0.22 ± 0.06**	**0.49**	**0.0038**	-0.09 ± 0.16	0.06	0.5977	0.09 ± 0.21	0.01	0.6787
3	-0.04 ± 0.03	0.10	0.2092	-0.38 ± 0.20	0.31	0.0950	**0.67 ± 0.21**	**0.47**	**0.0102**
4	**-0.24 ± 0.03**	**0.85**	**<0.0001**	0.06 ± 0.20	0.01	0.7621	**-0.47 ± 0.07**	**0.79**	**<0.0001**
5	**-0.15 ± 0.03**	**0.61**	**0.001**	**-0.44 ± 0.14**	**0.56**	**0.0124**	**0.44 ± 0.17**	**0.35**	**0.0212**
6	**-0.37 ± 0.05**	**0.86**	**<0.0001**	-0.02 ± 0.14	0.00	0.8698	-0.04 ± 0.10	0.01	0.6900
7	-0.27 ± 0.17	0.25	0.1402						
Fit Average	**-0.25 ± 0.03**	**0.88**	**<0.0001**	**-0.27 ± 0.10**	**0.46**	**0.0305**	0.11 ± 0.17	0.05	0.5538
Slope Dist ≠ 0	**-0.20 ± 0.04**	**-**	**0.0021**	**-0.16 ± 0.08**	**-**	**0.0658**	0.13 ± 0.16	-	0.3700

687

688 **Table 1: Linear regression slope values for fits to normalized density of three classes of**
689 **interneuron versus RC distance in individual mice.** Bold values correspond to significant ($p<0.05$)
690 slope values (mm^{-1}). Linear regression was also performed on the average normalized density across
691 mice versus distance for each interneuron class (Fit Average). P-values correspond to tests for slope
692 not equal to zero. Finally, the distribution of slope values was compared to zero using a non-parametric
693 Mann-Whitney test (distribution ≠ 0). SST- somatostatin interneurons, PV- parvalbumin interneurons,
694 CB- Calbindin interneurons.

695

696

697

698

699

700

701

702

703

704

705

706

707

708

bioRxiv preprint doi: https://doi.org/10.1101/152975; this version posted July 31, 2017. The copyright holder for this preprint (which was not certified by peer review) is the author/funder, who has granted bioRxiv a license to display the preprint in perpetuity. It is made available under aCC-BY 4.0 International license.

709

Layer 2	HC			HCO			NEO		
Mouse	Slope	R^2	P	Slope	R^2	P	Slope	R^2	P
1	0.11 ± 0.21	0.03	0.6000	-0.02 ± 0.10	0.01	0.7864	**-0.32 ± 0.13**	**0.29**	**0.0276**
2	-0.14 ± 0.12	0.09	0.2700	-0.40 ± 0.37	0.09	0.3000	0.17 ± 0.26	0.05	0.5100
3	0.60 ± 0.52	0.12	0.2700	-0.17 ± 0.11	0.18	0.1250	-0.18 ± 0.17	0.12	0.3220
4	**1.62 ± 0.38**	**0.61**	**0.0009**	**0.30 ± 0.13**	**0.27**	**0.0370**	-0.08 ± 0.08	0.12	0.3297
5	0.22 ± 0.31	0.04	0.5300	0.10 ± 0.27	0.01	0.7000	**-0.10 ± 0.02**	**0.63**	**0.0032**
6	-0.06 ± 0.13	0.02	0.6400	0.07 ± 0.10	0.04	0.4800	0.0008 ± 0.07	0.00	0.9914
Fit Average	**0.42 ± 0.10**	**0.58**	**0.0016**	-0.06 ± 0.06	0.08	0.2972	-0.09 ± 0.09	0.06	0.3500
Slope Dist ≠ 0	0.39 ± 0.27	-	0.3789	0.01 ± 0.10	-	0.3789	-0.08 ± 0.07	-	0.0658

Layer 3	HC			HCO			NEO		
Mouse	Slope	R^2	P	Slope	R^2	P	Slope	R^2	P
1	**-0.34 ± 0.12**	**0.42**	**0.0224**	**-0.24 ± 0.10**	**0.32**	**0.0330**	**-0.68 ± 0.08**	**0.84**	**<0.0001**
2	-0.16 ± 0.11	0.14	0.17	-0.36 ± 0.33	0.11	0.3100	**-0.37 ± 0.08**	**0.72**	**0.0018**
3	0.37 ± 0.27	0.16	0.2138	-0.22 ± 0.13	0.20	0.1100	**-0.34 ± 0.09**	**0.79**	**0.0060**
4	0.33 ± 0.44	0.04	0.47	-0.11 ± 0.20	0.02	0.5900	**-0.52 ± 0.08**	**0.84**	**0.0002**
5	0.55 ± 0.25	0.33	0.053	-0.03 ± 0.14	0.00	0.8000	**-0.39 ± 0.09**	**0.66**	**0.0023**
6	0.02 ± 0.27	0.00	0.9427	**-0.29 ± 0.10**	**0.37**	**0.0120**	**-0.39 ± 0.08**	**0.64**	**0.0003**
Fit Average	0.20 ± 0.11	0.21	0.11	**-0.19 ± 0.04**	**0.58**	**0.0005**	**-0.47 ± 0.04**	**0.94**	**<0.0001**
Slope Dist ≠ 0	0.13 ± 0.14	-	0.3789	**-0.21 ± 0.05**	**-**	**0.0050**	**-0.45 ± 0.05**	**-**	**0.0050**

710

711 **Table 2: Linear regression slope values for fits to normalized density of tdTom(+) cells versus**
712 **RC distance in individual mice.** Bold values correspond to significant ($p<0.05$) slope values (mm^{-1}).
713 Underlined values correspond to the cohort of mice exposed to ethyl butyrate (HCO, NEO only) and the
714 remaining mice were exposed isoamyl acetate. Linear regression was also performed on the average
715 normalized density across mice versus distance (Fit Average). P-values correspond to tests for slope
716 not equal to zero. Finally, the distribution of slope values was compared to zero using a non-parametric
717 Mann-Whitney test (distribution ≠ 0). HC- home cage, HCO- home cage plus odor, NEO- novel
718 environment plus odor.

719

720

721

bioRxiv preprint doi: https://doi.org/10.1101/152975; this version posted July 31, 2017. The copyright holder for this preprint (which was not certified by peer review) is the author/funder, who has granted bioRxiv a license to display the preprint in perpetuity. It is made available under aCC-BY 4.0 International license.

722 **Figure Legends**

723 **Figure 1: Caudally biased, asymmetric inhibition of pyramidal cells in APC. A)** Schematic of grid-
724 stimulation paradigm for L2 excitatory neurons- semilunar cells (SL) and superficial (s) pyramidal cells
725 (sPCs). VG- interneuron expressing ChR2 under VGAT promoter. R: rostral, C: caudal. **B1)** IPSCs
726 recorded during focal light stimulation at each grid location in a representative SL cell. Scale bars:
727 vertical 100 pA, horizontal 200 ms. Red trace indicates location of recorded cell. **B2)** Bias values are
728 uniformly distributed across SL cells. Negative values correspond to greater average inhibition from
729 rostral sites and positive values correspond to greater inhibition from caudal sites. **C1)** IPSCs recorded
730 from a representative L2 sPC. **C2)** Predominantly positive bias values in sPCs indicates stronger
731 inhibition from caudal versus rostral sites (* $p<0.05$, n=14, one sample t-test). Scale bars: vertical 100
732 pA, horizontal 200 ms. **D1)** Schematic of grid-stimulation paradigm for L3 deep pyramidal cells (dPCs).
733 **D2)** IPSCs recorded from a representative L3 dPC. Scale bars: vertical 200 pA, horizontal 200 ms. **D3)**
734 Predominantly positive bias values in dPCs indicates stronger inhibition from caudal versus rostral sites
735 (** $p<0.01$, n=16, one sample t-test). **E1)** Recordings of two dPCs in the same slice indicate that the
736 caudal (C) neuron of a pair receives stronger inhibition than the rostral (R) neuron (** $p<0.01$, n=19
737 pairs, paired t-test). IPSCs were evoked using a 70 μm light spot centered on the soma of the recorded
738 PC. **E2)** The difference in inhibition (pAs) between the caudal (C) and rostral (R) cell in each pair (E1)
739 is plotted against the difference in RC distance between the two cells. As the distance between the two
740 cells increases, the difference in inhibition also increases (* $p<0.05$, linear regression, n=19). **F)**
741 Inhibitory strength versus RC position of the dPC relative to the rostral start of the LOT in the sagittal
742 slice. Inhibition increases with RC distance (** $p<0.01$, linear regression, n=27).

743 **Figure 2: Rostrally biased, asymmetric inhibition of L3 interneurons. A)** Schematic of grid-
744 stimulation paradigm for L2 and L3 inhibitory neurons (INT). **B)** Inhibition is significantly stronger in L3
745 INT (filled green circles) than L2 INT (** $p<0.01$, ANOVA, open green circles) but did not significantly
746 differ from L3 dPCs (solid black triangles). Values correspond to the maximum IPSC for each cell
747 regardless of location in grid. **C1)** IPSCs recorded during focal light stimulation at each grid location in

bioRxiv preprint doi: https://doi.org/10.1101/152975; this version posted July 31, 2017. The copyright holder for this preprint (which was not certified by peer review) is the author/funder, who has granted bioRxiv a license to display the preprint in perpetuity. It is made available under aCC-BY 4.0 International license.

748 a representative L2 INT. Scale bars: vertical 100 pA, horizontal 200 ms. Red trace indicates location of
749 recorded cell. **C2)** The bias values for L2 INTs do not differ from zero. **D1)** IPSCs recorded from a
750 representative L3 INT. Scale bars: vertical 200 pA, horizontal 200 ms. **D2)** Asymmetric distribution of
751 bias values in dPCs indicates stronger inhibition from rostral versus caudal sites (** $p<0.05$, n=25, one
752 sample t-test). **E)** The bias values of dPCs (black triangles) significantly differed from L3 INTs (**
753 $p<0.01$, unpaired t-test, green circles). **F)** Average inhibitory strength across rostral (I_R) or caudal (I_C)
754 sites in dPCs (black triangles) and L3 INT (green circles). Opposing inhibitory asymmetries: in dPCs,
755 average I_C was significantly greater than I_R (black ** $p<0.01$ paired t-test), while I_R was significantly
756 greater than I_C I in L3 INTs (green ** $p<0.01$, paired t-test).

757 **Figure 3: Rostral-caudal distributions of L3 interneurons. A1)** Representative coronal sections from
758 rostral (0-200 µm, left) and caudal (within last 300 µm, right) APC showing SST-tdTom(+) cells in L3
759 region of interest (ROI, dashed line). Scale bar: 500 µm **A2)** Normalized density versus RC distance for
760 the mouse shown in A1 (SST-mouse #2, **Table 1**, ** $p<0.01$. **A3)** Normalized density of SST-cells
761 versus distance for all mice (open circles). The average (± SE, n=7) normalized density of SST cells
762 across mice significantly decreased with RC distance (red circles, **$p<0.01$). **A4)** Distribution of slopes
763 from linear fits to data from individual mice. Solid circles indicate significantly negative slopes ($p<0.05$).
764 The distribution of slope values was significantly non-zero (** p: 0.002 MWU-test). **B1-4)** As in A1-4,
765 except for Calbindin(+) interneurons (CB). **B1,2)** Data from CB mouse #5 in **Table 1**. **B3**) On average,
766 there is no change in density of CB cells along the RC axis (filled green circles, p: 0.55). **B4)** In
767 individual mice CB cells significantly increased or decreased (filled green circles) along the RC axis, but
768 the distribution of slopes did not differ from zero (p: 0.37, MWU-test). **C1-4)** As in A1-4, except for
769 Parvalbumin(+) interneurons (PV). **B1,2)** Data from PV mouse #6 in **Table 1**. **C3**) On average, the
770 density of PV cells decreased along the RC axis (filled black circles, p: 0.03). **C4)** However, only one
771 mouse showed a significant decrease in PV cells along the RC axis (filled black circle) and the
772 distribution of slopes did not differ from zero (p: 0.07, MWU-test).

bioRxiv preprint doi: https://doi.org/10.1101/152975; this version posted July 31, 2017. The copyright holder for this preprint (which was not certified by peer review) is the author/funder, who has granted bioRxiv a license to display the preprint in perpetuity. It is made available under aCC-BY 4.0 International license.

773 **Figure 4: Spatial profiles of SST-cell mediated inhibition of L3 pyramidal cells and interneurons.**
774 **A)** Schematic of grid-stimulation paradigm for L3 dPCs and inhibitory neurons (INT) in sagittal sections
775 from SST-ChR2 mice. **B1)** IPSCs recorded during focal light stimulation at each grid location in a
776 representative L3 INT. Scale bars: vertical 200 pA, horizontal 200 ms. Red trace indicates location of
777 recorded cell. **B2)** The distribution of bias values for L3 INTs is significantly rostrally biased (*$p<0.05$,
778 one sample t-test, blue line) and does not differ from VGAT-ChR2 animals (green line). **C1)** IPSCs
779 recorded from a representative L3 dPC. Scale bars: vertical 100 pA, horizontal 200 ms. **C2)** The
780 distribution of bias values in dPCs is not asymmetric with a mean near zero (blue line) compared to a
781 caudally biased mean in VGAT-ChR2 animals (green line). **D)** Normalized inhibition on rostral versus
782 caudal sides in VGAT-ChR2 (green) and SST-ChR2 (blue) mice is significantly asymmetric and
783 rostrally biased in L3 interneurons (circles, Left). SST-ChR2 mediated inhibition is not significantly
784 asymmetric in dPCs (right triangles, SST-ChR2: blue, VGAT-ChR2: green). **E)** Schematic of
785 optogenetic stimulation of VGAT-ChR2(+) interneurons (green) including SST-cells which also express
786 the inhibitory DREADD, (SST-Di, black with green outline). **F)** IPSCs in response to optogenetic
787 activation of L3 rostral and caudal sites in control (green) and CNO (black). **G)** Change in RC bias
788 ($Bias_{CNO}$-$Bias_{Pre}$) in the presence of CNO. Inhibition became less caudally biased in n=8 cells (negative
789 values, black bars) in CNO but more caudally biased in n=4 cells (positive values, gray bars).

790 **Figure 5: Spatial profiles of neural activity in APC following odor exposure. A)** tdTom(+) cells
791 from a Fos^{ERT}xAi14 mouse in rostral (left) and caudal (right) sections from (NEO condition). Dashed
792 lines delineate Layers 2 and 3 and the lateral olfactory tract (lot). DAPI stain for nuclei (blue). **B1, B2)**
793 Schematics of experimental schedule (**B1**) and contexts **(B2)**. Abbreviations: HC: home cage, HCO:
794 home cage plus odor, NEO: Novel environment plus odor, 4-OHT: 4-hydroxytamoxifen. **B3**) Location of
795 an example mouse in the NEO arena during 30 min odor exposure. Mice continuously move between
796 the odorized (orange circle (+)) and non-odor arms (blank circle (-)) as well as the center (C) of the
797 arena. **C, D)** Normalized density of tdTom(+) cells along the RC axis of L2 **(C)** and L3 (**D**)**.** Open
798 triangles: data from individual animals; filled triangles: average across animals. **E)** Slopes of linear fits

bioRxiv preprint doi: https://doi.org/10.1101/152975; this version posted July 31, 2017. The copyright holder for this preprint (which was not certified by peer review) is the author/funder, who has granted bioRxiv a license to display the preprint in perpetuity. It is made available under aCC-BY 4.0 International license.

799 to density versus distance for individual mice in each condition in L2 (**E1**) and L3 (**E2**). Filled triangles
800 indicate slopes significantly different from zero ($p<0.05$, see **Table 1** for p: values). **E2**) In L3, the
801 distribution of slopes in HCO and NEO animals significantly differed from 0 (** $p<0.01$, MWU-test).
802 Further the distribution of slopes in NEO animals significantly differed from HC and HCO animals (★★
803 $p<0.01$, KW-test). **F)** The average density of neurons increases with odor exposure (HCO, NEO) in L2
804 (**F1, *** $p<0.05$, KW-test) but not L3 **(F2)**.

805 **Figure 6: The spatial profiles of inhibition are commensurate with neural activity along the RC**
806 **axis of APC. A1)** Schematic summarizing rostral-caudal spatial profiles of inhibition (green), SST-
807 interneuron density and SST-mediated inhibition of interneurons (blue) and active neurons in L3 of
808 NEO mice (red). **A2)** Proposed disinhibitory circuit consisting of a higher density of rostral SST-cells
809 (blue) that inhibit interneurons (light green) and disinhibit PCs increasing rostral neural activity (red
810 PCs). In caudal APC, lower density of SST-cells allows greater inhibition (dark green) and less active
811 PCs (black). **B)** Normalized density of active neurons (red triangles) decreases along the RC axis
812 (slope: -0.47 mm^{-1}, R^2:0.94, $p<0.0001$, from **Figure 5D3**), as normalized inhibition of dPCs increases
813 (slope: +0.67 mm^{-1}, R^2:0.95, $p<0.0001$, from **Figure 1F**). Because there are only two points at 1.5 mm
814 in **Figure 1F**, inhibitory strength was normalized to a projected "maximum" strength (8.17 pAs) at 1.6
815 mm, based on the linear fit to inhibitory strength versus distance.

816

817

818

819

820

821

822

823

bioRxiv preprint doi: https://doi.org/10.1101/152975; this version posted July 31, 2017. The copyright holder for this preprint (which was not certified by peer review) is the author/funder, who has granted bioRxiv a license to display the preprint in perpetuity. It is made available under aCC-BY 4.0 International license.

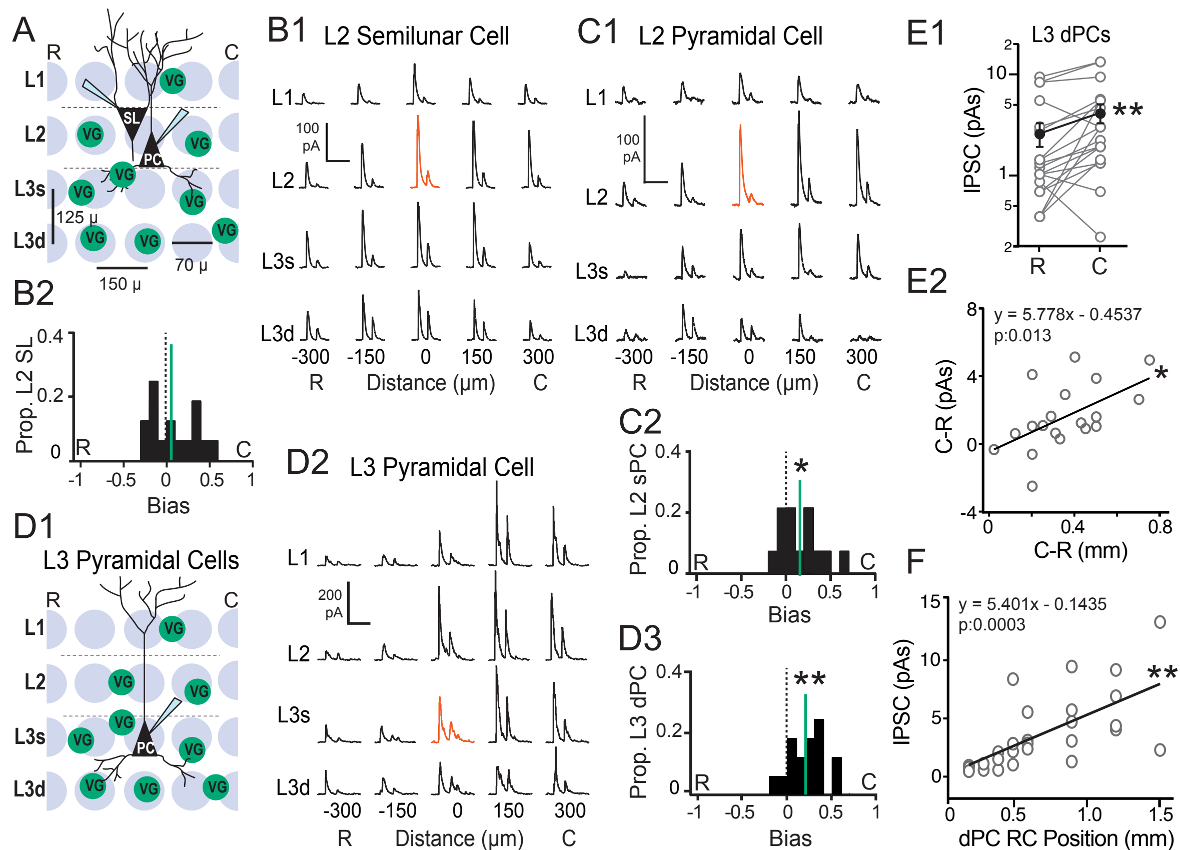

Figure 1: Caudally biased, asymmetric inhibition of pyramidal cells in APC. A) Schematic of grid-stimulation paradigm for L2 excitatory neurons- semilunar cells (SL) and superficial (s) pyramidal cells (sPCs). VG- interneuron expressing ChR2 under VGAT promoter. R: rostral, C: caudal. B1) IPSCs recorded during focal light stimulation at each grid location in a representative SL cell. Scale bars: vertical 100 pA, horizontal 200 ms. Red trace indicates location of recorded cell. B2) Bias values are uniformly distributed across SL cells. Negative values correspond to greater average inhibition from rostral sites and positive values correspond to greater inhibition from caudal sites. C1) IPSCs recorded from a representative L2 sPC. C2) Predominantly positive bias values in sPCs indicates stronger inhibition from caudal versus rostral sites (* $p<0.05$, n=14, one sample t-test). Scale bars: vertical 100 pA, horizontal 200 ms. D1) Schematic of grid-stimulation paradigm for L3 deep pyramidal cells (dPCs). D2) IPSCs recorded from a representative L3 dPC. Scale bars: vertical 200 pA, horizontal 200 ms. D3) Predominantly positive bias values in dPCs indicates stronger inhibition from caudal versus rostral sites (** $p<0.01$, n=16, one sample t-test). E1) Recordings of two dPCs in the same slice indicate that the caudal (C) neuron of a pair receives stronger inhibition than the rostral (R) neuron (**$p<0.01$, n=19 pairs, paired t-test). IPSCs were evoked using a 70 μm light spot centered on the soma of the recorded PC. E2) The difference in inhibition (pAs) between the caudal (C) and rostral (R) cell in each pair (E1) is plotted against the difference in RC distance between the two cells. As the distance between the two cells increases, the difference in inhibition also increases (* $p<0.05$, linear regression, n=19). F) Inhibitory strength versus RC position of the dPC relative to the rostral start of the LOT in the sagittal slice. Inhibition increases with RC distance (**$p<0.01$, linear regression, n=27).

bioRxiv preprint doi: https://doi.org/10.1101/152975; this version posted July 31, 2017. The copyright holder for this preprint (which was not certified by peer review) is the author/funder, who has granted bioRxiv a license to display the preprint in perpetuity. It is made available under aCC-BY 4.0 International license.

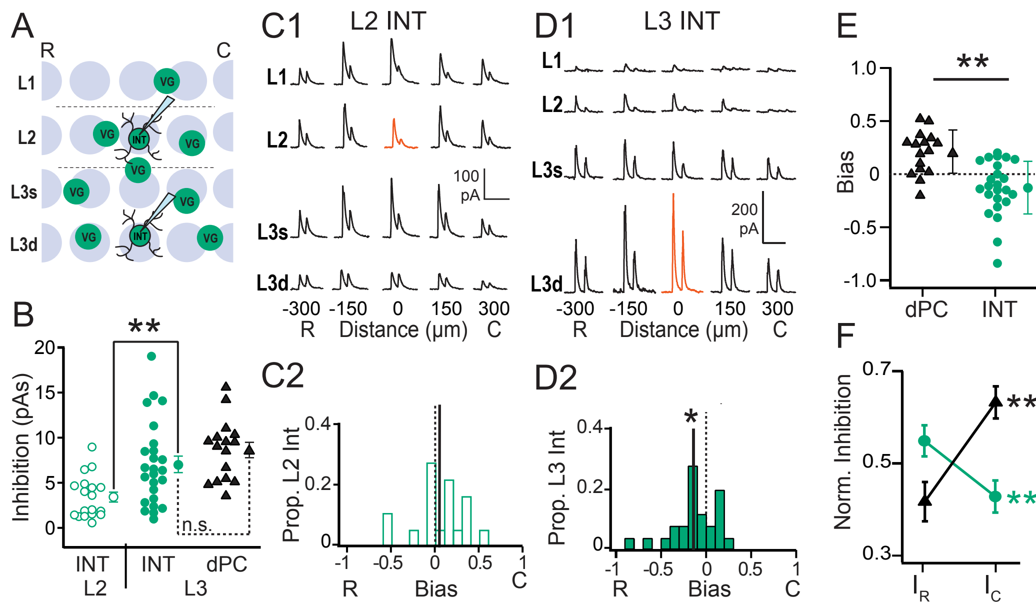

Figure 2: Rostrally biased, asymmetric inhibition of L3 interneurons. A) Schematic of grid-stimulation paradigm for L2 and L3 inhibitory neurons (INT). B) Inhibition is significantly stronger in L3 INT (filled green circles) than L2 INT (** p<0.01, ANOVA, open green circles) but did not significantly differ from L3 dPCs (solid black triangles). Values correspond to the maximum IPSC for each cell regardless of location in grid. C1) IPSCs recorded during focal light stimulation at each grid location in a representative L2 INT. Scale bars: vertical 100 pA, horizontal 200 ms. Red trace indicates location of recorded cell. C2) The bias values for L2 INTs do not differ from zero. D1) IPSCs recorded from a representative L3 INT. Scale bars: vertical 200 pA, horizontal 200 ms. D2) Asymmetric distribution of bias values in dPCs indicates stronger inhibition from rostral versus caudal sites (** p<0.05, n=25, one sample t-test). E) The bias values of dPCs (black triangles) significantly differed from L3 INTs (** p<0.01, unpaired t-test, green circles). F) Average inhibitory strength across rostral (IR) or caudal (IC) sites in dPCs (black triangles) and L3 INT (green circles). Opposing inhibitory asymmetries: in dPCs, average IC was significantly greater than IR (black ** p<0.01 paired t-test), while IR was significantly greater than IC I in L3 INTs (green ** p<0.01, paired t-test).

bioRxiv preprint doi: https://doi.org/10.1101/152975; this version posted July 31, 2017. The copyright holder for this preprint (which was not certified by peer review) is the author/funder, who has granted bioRxiv a license to display the preprint in perpetuity. It is made available under aCC-BY 4.0 International license.

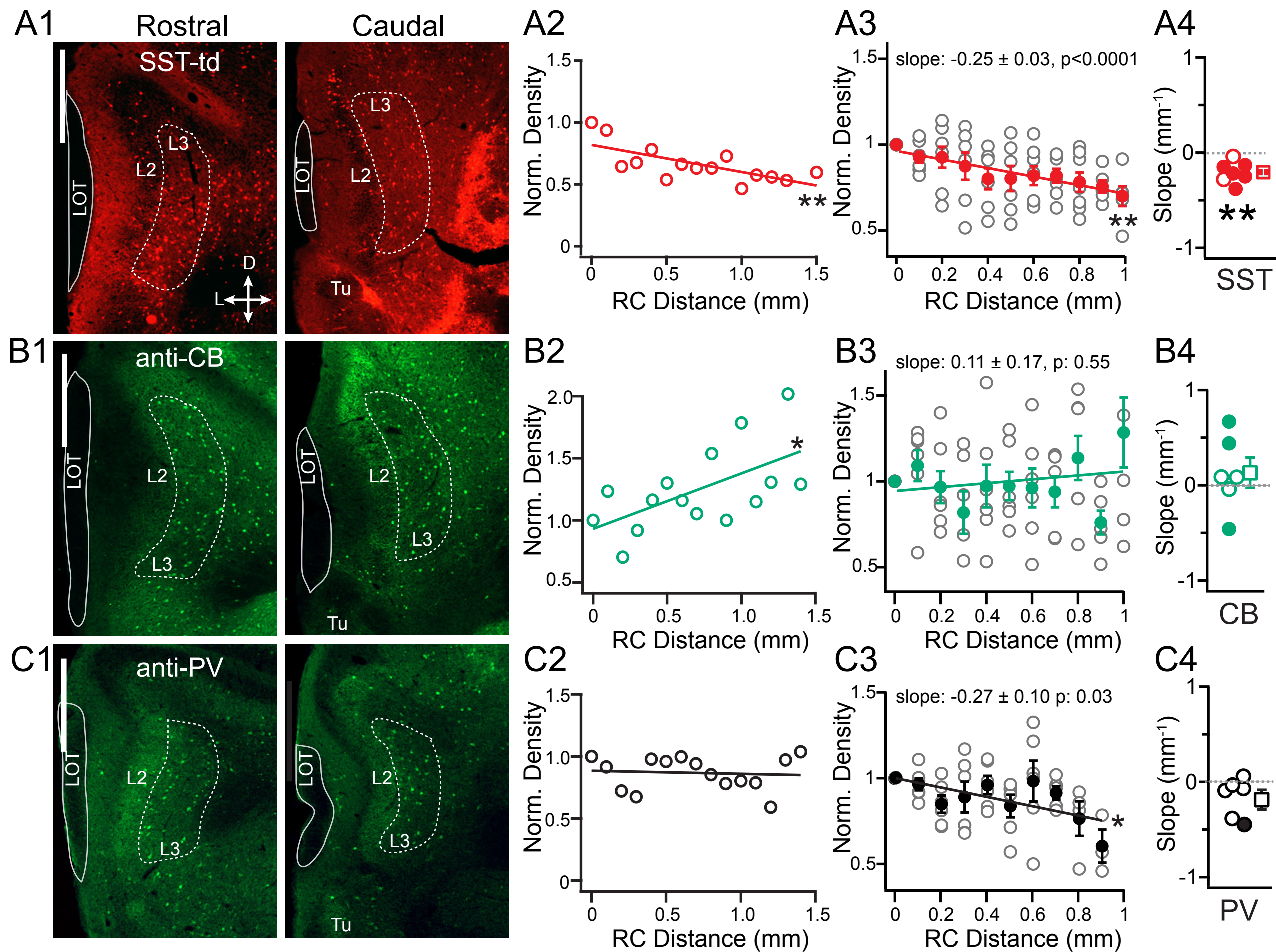

Figure 3: Rostral-caudal distributions of L3 interneurons. A1) Representative coronal sections from rostral (0-200 µm, left) and caudal (within last 300 µm, right) APC showing SST-tdTom(+) cells in L3 region of interest (ROI, dashed line). Scale bar: 500 µm A2) Normalized density versus RC distance for the mouse shown in A1 (SST-mouse #2, Table 1, ** $p<0.01$. A3) Normalized density of SST-cells versus distance for all mice (open circles). The average (± SE, n=7) normalized density of SST cells across mice significantly decreased with RC distance (red circles, ** $p<0.01$). A4) Distribution of slopes from linear fits to data from individual mice. Solid circles indicate significantly negative slopes ($p<0.05$). The distribution of slope values was significantly non-zero (** p: 0.002 MWU-test). B1-4) As in A1-4, except for Calbindin(+) interneurons (CB). B1,2) Data from CB mouse #5 in Table 1. B3) On average, there is no change in density of CB cells along the RC axis (filled green circles, p: 0.55). B4) In individual mice CB cells significantly increased or decreased (filled green circles) along the RC axis, but the distribution of slopes did not differ from zero (p: 0.37, MWU). C1-4) As in A1-4, except for Parvalbumin(+) interneurons (PV). B1,2) Data from PV mouse #6 in Table 1. C3) On average, the density of PV cells decreased along the RC axis (filled black circles, p: 0.03). C4) However, only one mouse showed a significant decrease in PV cells along the RC axis (filled black circle) and the distribution of slopes did not differ from zero (p: 0.07, MWU).

bioRxiv preprint doi: https://doi.org/10.1101/152975; this version posted July 31, 2017. The copyright holder for this preprint (which was not certified by peer review) is the author/funder, who has granted bioRxiv a license to display the preprint in perpetuity. It is made available under aCC-BY 4.0 International license.

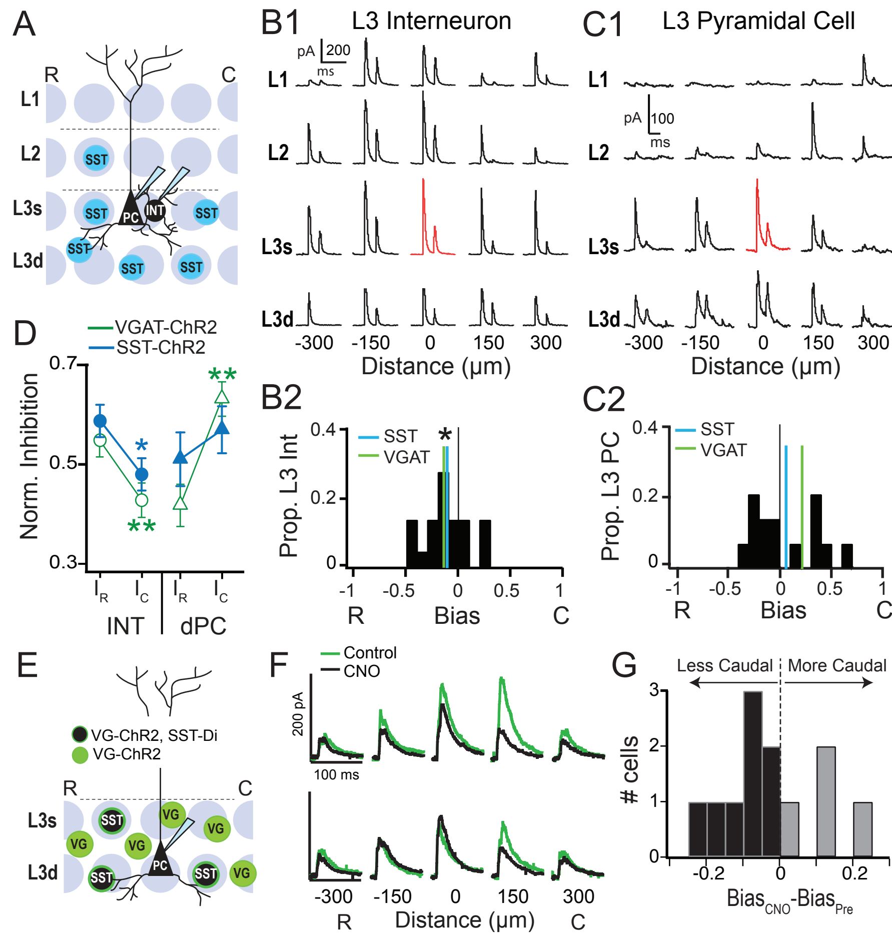

Figure 4: Spatial profiles of SST-cell mediated inhibition of L3 pyramidal cells and interneurons. A) Schematic of grid-stimulation paradigm for L3 dPCs and inhibitory neurons (INT) in sagittal sections from SST-ChR2 mice. B1) IPSCs recorded during focal light stimulation at each grid location in a representative L3 INT. Scale bars: vertical 200 pA, horizontal 200 ms. Red trace indicates location of recorded cell. B2) The distribution of bias values for L3 INTs is significantly rostrally biased (*p<0.05, one sample t-test, blue line) and does not differ from VGAT-ChR2 animals (green line). C1) IPSCs recorded from a representative L3 dPC. Scale bars: vertical 100 pA, horizontal 200 ms. C2) The distribution of bias values in dPCs is not asymmetric with a mean near zero (blue line) compared to a caudally biased mean in VGAT-ChR2 animals (green line). D) Normalized inhibition on rostral versus caudal sides in VGAT-ChR2 (green) and SST-ChR2 (blue) mice is significantly asymmetric and rostrally biased in L3 interneurons (circles, Left). SST-ChR2 mediated inhibition is not significantly asymmetric in dPCs (right triangles, SST-ChR2: blue, VGAT-ChR2: green). E) Schematic of optogenetic stimulation of VGAT-ChR2(+) interneurons (green) including SST-cells which also express the inhibitory DREADD, (SST-Di, black with green outline). F) IPSCs in response to optogenetic activation of L3 rostral and caudal sites in control (green) and CNO (black). G) Change in RC bias (BiasCNO-BiasPre) in the presence of CNO. Inhibition became less caudally biased in n=8 cells (negative values, black bars) in CNO but more caudally biased in n=4 cells (positive values, gray bars).

bioRxiv preprint doi: https://doi.org/10.1101/152975; this version posted July 31, 2017. The copyright holder for this preprint (which was not certified by peer review) is the author/funder, who has granted bioRxiv a license to display the preprint in perpetuity. It is made available under aCC-BY 4.0 International license.

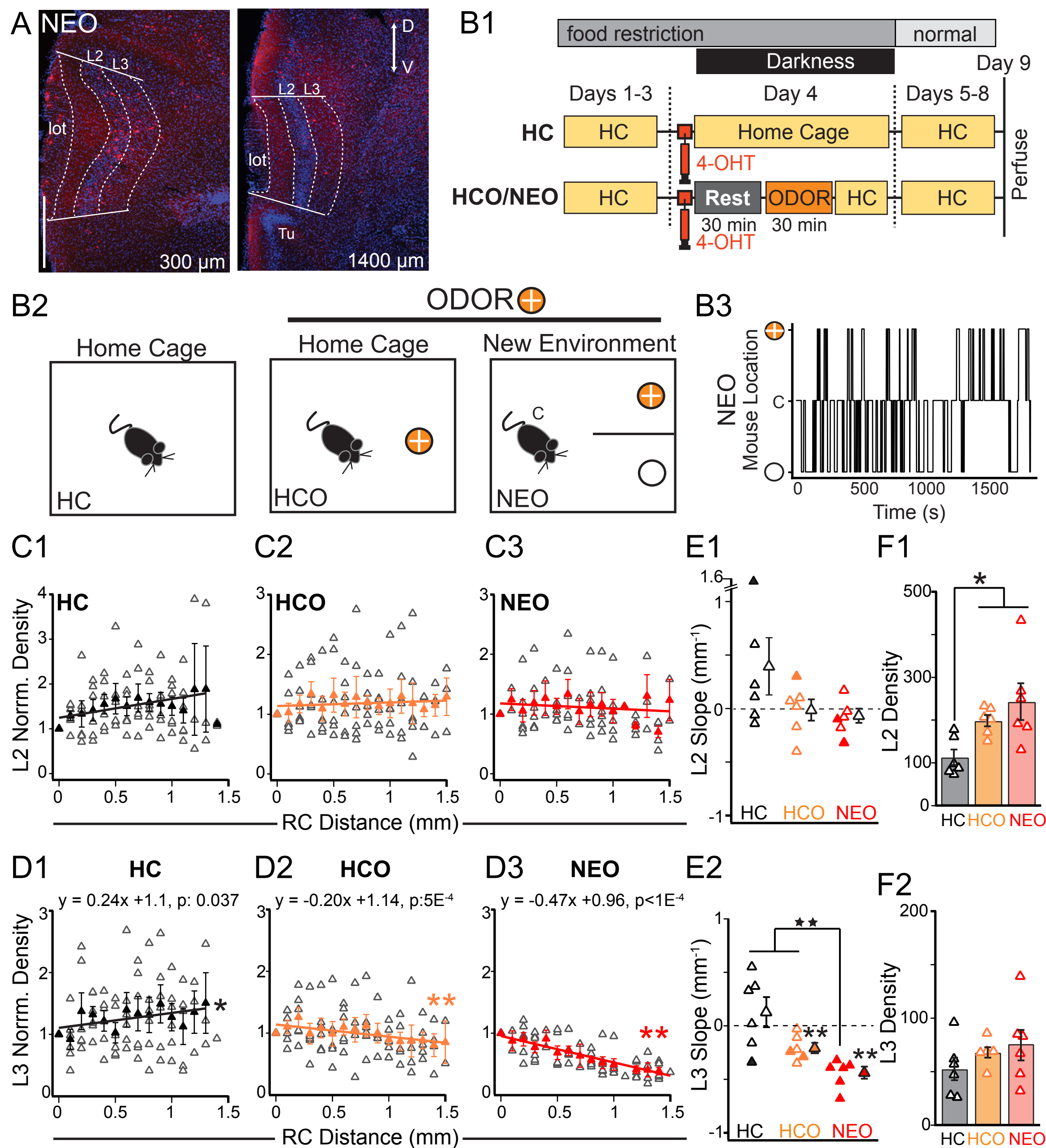

Figure 5: Spatial profiles of neural activity in APC following odor exposure. A) tdTom(+) cells from a FosERTxAi14 mouse in rostral (left) and caudal (right) sections from (NEO condition). Dashed lines delineate Layers 2 and 3 and the lateral olfactory tract (lot). DAPI stain for nuclei (blue). B1, B2) Schematics of experimental schedule (B1) and contexts (B2). Abbreviations: HC: home cage, HCO: home cage plus odor, NEO: Novel environment plus odor, 4-OHT: 4-hydroxytamoxifen. B3) Location of an example mouse in the NEO arena during 30 min odor exposure. Mice continuously move between the odorized (orange circle (+)) and non-odor arms (blank circle (-)) as well as the center (C) of the arena. C, D) Normalized density of tdTom(+) cells along the RC axis of L2 (C) and L3 (D). Open triangles: data from individual animals; filled triangles: average across animals. E) Slopes of linear fits to density versus distance for individual mice in each condition in L2 (E1) and L3 (E2). Filled triangles indicate slopes significantly different from zero ($p<0.05$, see Table 1 for p: values). E2) In L3, the distribution of slopes in HCO and NEO animals significantly differed from 0 (** $p<0.01$, MWU-test). Further the distribution of slopes in NEO animals significantly differed from HC and HCO animals (⋆⋆ $p<0.01$, KW-test). F) The average density of neurons increases with odor exposure (HCO, NEO) in L2 (F1, * $p<0.05$, KW-test) but not L3 (F2).

bioRxiv preprint doi: https://doi.org/10.1101/152975; this version posted July 31, 2017. The copyright holder for this preprint (which was not certified by peer review) is the author/funder, who has granted bioRxiv a license to display the preprint in perpetuity. It is made available under aCC-BY 4.0 International license.

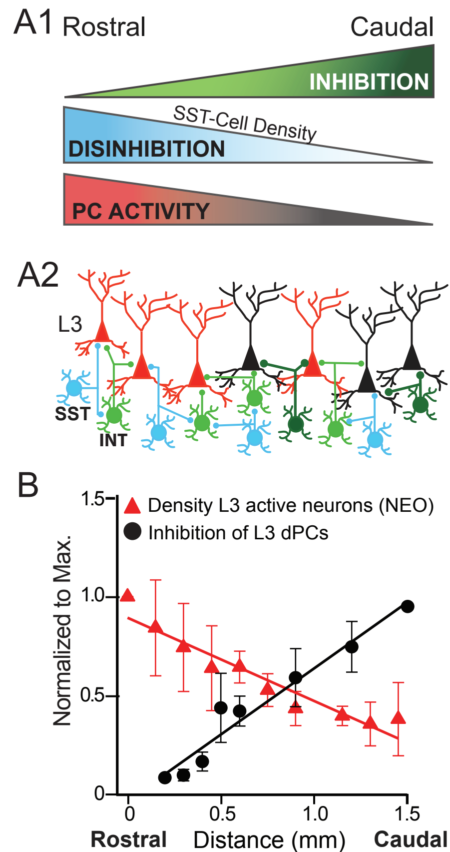

Figure 6: The spatial profiles of inhibition are commensurate with neural activity along the RC axis of APC. A1) Schematic summarizing rostral-caudal spatial profiles of inhibition (green), SST-interneuron density and SST-mediated inhibition of interneurons (blue) and active neurons in L3 of NEO mice (red). A2) Proposed disinhibitory circuit consisting of a higher density of rostral SST-cells (blue) that inhibit interneurons (light green) and disinhibit PCs increasing rostral neural activity (red PCs). In caudal APC, lower density of SST-cells allows greater inhibition (dark green) and less active PCs (black). B) Normalized density of active neurons (red triangles) decreases along the RC axis (slope: -0.47 mm-1, R^2: 0.94, $p<0.0001$, from Figure 5D3), as normalized inhibition of dPCs increases (slope: +0.67 mm-1, R^2: 0.95, $p<0.0001$, from Figure 1F). Because there are only two points at 1.5 mm in Figure 1F, inhibitory strength was normalized to a projected "maximum" strength (8.17 pAs) at 1.6 mm, based on the linear fit to inhibitory strength versus

bioRxiv preprint doi: https://doi.org/10.1101/152975; this version posted July 31, 2017. The copyright holder for this preprint (which was not certified by peer review) is the author/funder, who has granted bioRxiv a license to display the preprint in perpetuity. It is made available under aCC-BY 4.0 International license.

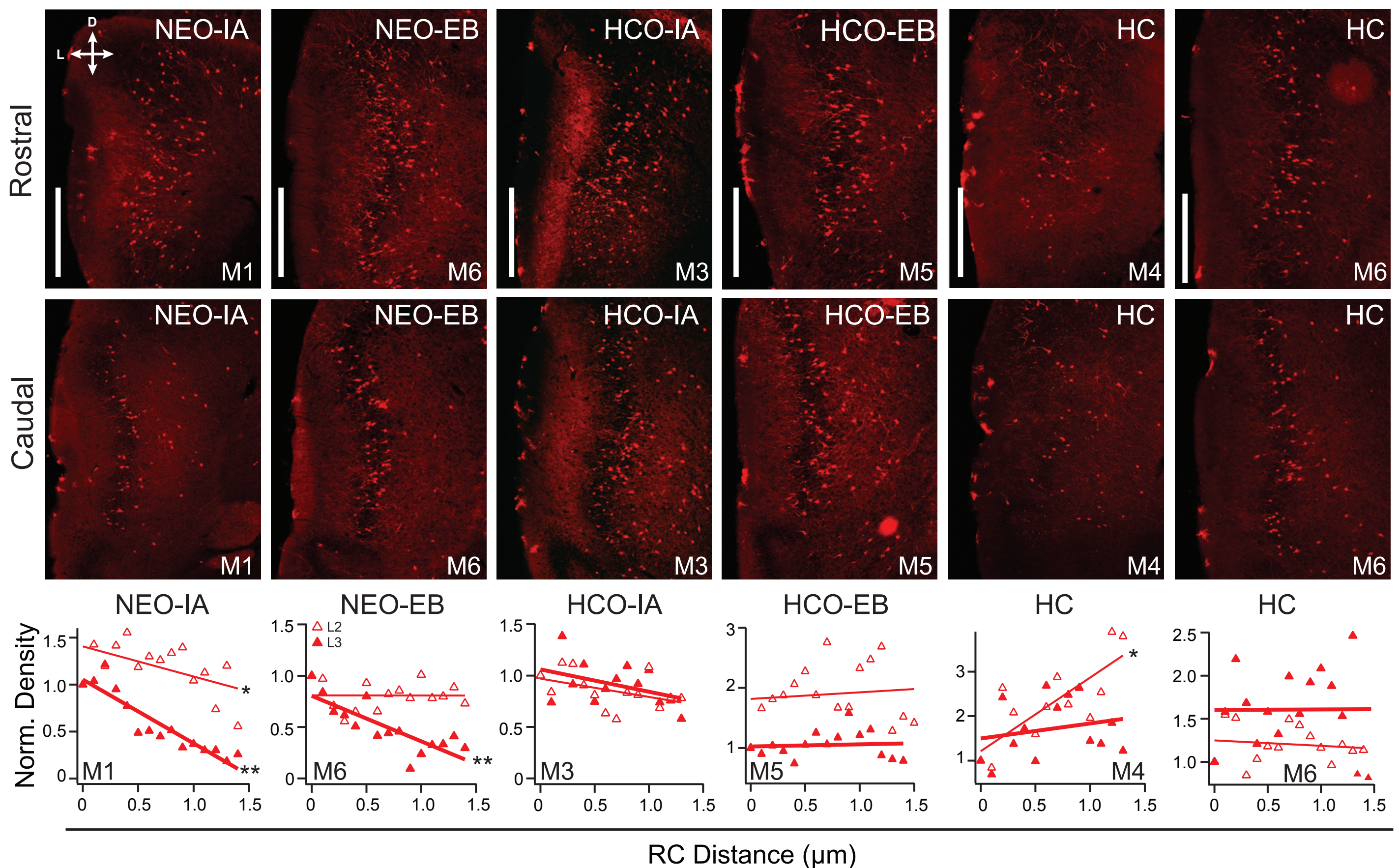

Supplemental Figure 1: Fos-tdTom(+) cells in anterior piriform cortex (APC) . Representative coronal sections from the rostral (0-200 µm, upper row) and caudal (within last 300 µm, middle row) APC showing fos-tdTom(+) cells activated during novel odor exposure in a novel environment (NEO) or the home cage (HCO), or the home cage with no odor (HC). Bottom row: Normalized density (Layer 2, open triangles, L3 filled triangles) versus distance along the RC axis of Fos-tdTom(+) cells for the mouse corresponding to the sections above. Linear regression fits (thin lines, L2: thick lines, L3) with slopes that significantly differed from zero are indicated by astrisks: * $p<0.05$, or ** $p<0.01$. Each column is data from an individual mouse and the mouse number (M1-6) matches the mouse numbers in Table 2 (main text). Responses to isoamyl-acetate (IA, left) or ethyl butyrate (EB, right) are shown for each odor condition.

bioRxiv preprint doi: https://doi.org/10.1101/152975; this version posted July 31, 2017. The copyright holder for this preprint (which was not certified by peer review) is the author/funder, who has granted bioRxiv a license to display the preprint in perpetuity. It is made available under aCC-BY 4.0 International license.

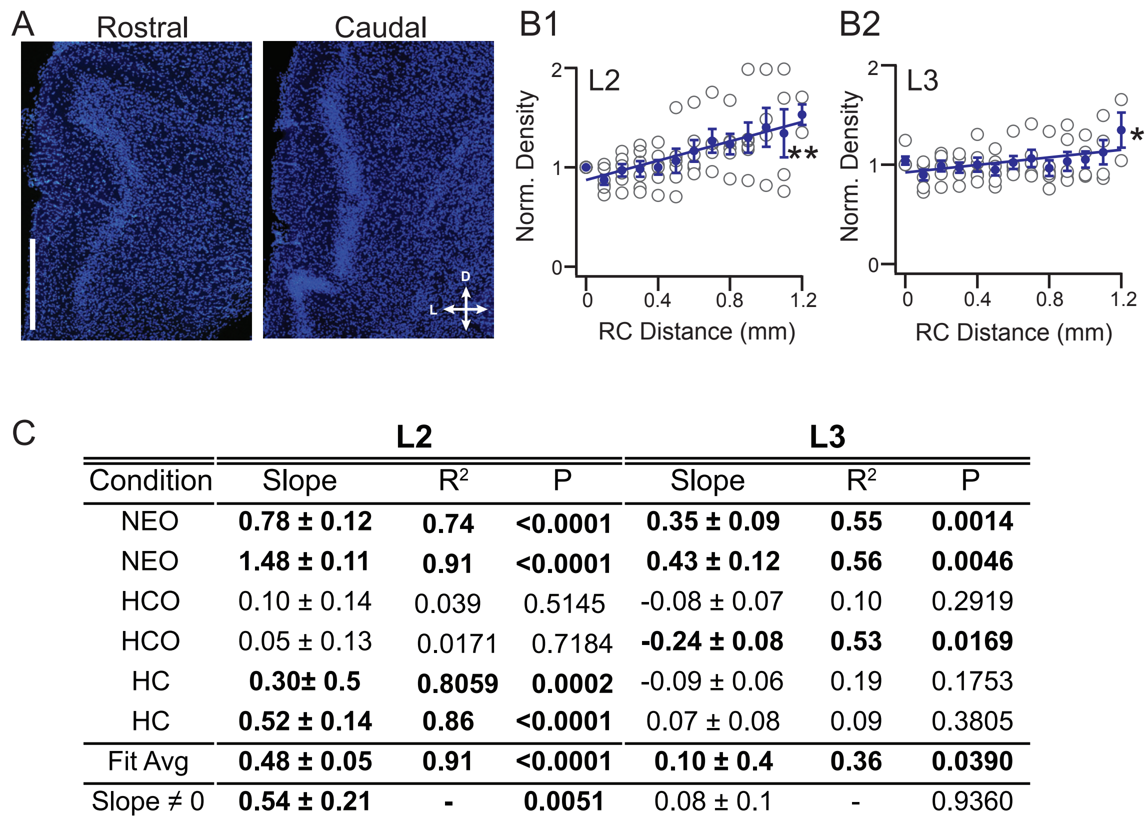

Condition	L2 Slope	L2 R^2	L2 P	L3 Slope	L3 R^2	L3 P
NEO	**0.78 ± 0.12**	**0.74**	**<0.0001**	**0.35 ± 0.09**	**0.55**	**0.0014**
NEO	**1.48 ± 0.11**	**0.91**	**<0.0001**	**0.43 ± 0.12**	**0.56**	**0.0046**
HCO	0.10 ± 0.14	0.039	0.5145	-0.08 ± 0.07	0.10	0.2919
HCO	0.05 ± 0.13	0.0171	0.7184	**-0.24 ± 0.08**	**0.53**	**0.0169**
HC	**0.30± 0.5**	**0.8059**	**0.0002**	-0.09 ± 0.06	0.19	0.1753
HC	**0.52 ± 0.14**	**0.86**	**<0.0001**	0.07 ± 0.08	0.09	0.3805
Fit Avg	**0.48 ± 0.05**	**0.91**	**<0.0001**	**0.10 ± 0.4**	**0.36**	**0.0390**
Slope ≠ 0	**0.54 ± 0.21**	**-**	**0.0051**	0.08 ± 0.1	-	0.9360

Supplemental Figure 2: DAPI staining in anterior piriform cortex (APC) . Representative coronal sections from rostral (0-200 µm, upper row) and caudal (within last 300 µm) APC showing DAPI(+) nuclei from mice exposed to novel odor exposure in a novel environment (NEO). B) Bottom row: Normalized density versus distance along the RC axis of DAPI(+) cells for individual mice (open circles) and average across mice (blue filled circles) in L2 (B1) and L3 (B2). Linear regression fits of average data have slopes that significantly differed from zero are indicated by astrisks: * $p<0.05$, or ** $p<0.01$. C) Table with slope (mm^{-1}) data and statistics for each animal. Bold numbers correspond to significant slopes ($p<0.05$). Fit average corresponds to the linear fits shown in (B). The slope distribution was significantly different from zero for L2 but not L3. HCO: home cage + odor, or the home cage with no odor (HC). Scale: 500 µm

bioRxiv preprint doi: https://doi.org/10.1101/152975; this version posted July 31, 2017. The copyright holder for this preprint (which was not certified by peer review) is the author/funder, who has granted bioRxiv a license to display the preprint in perpetuity. It is made available under aCC-BY 4.0 International license.

Location		Distribution ≠ 0	mean	SD	Test	p	n	α: 0.05 1-β
Figure 1		bias SL ≠ 0	0.08	0.40	1 sample t-test	0.490	13	0.12
		bias sPC ≠ 0	0.22	0.30	1 sample t-test	**0.016**	14	0.85
		bias dPC ≠ 0	0.19	0.20	1 sample t-test	**0.001**	16	0.9673
Figure 2		bias L2 INT ≠ 0	0.04	0.30	1 sample t-test	0.110	18	0.09
		bias L3 INT ≠ 0	-0.13	0.25	1 sample t-test	**0.013**	25	0.74
Figure 4		bias L3 INT ≠ 0 SST	-0.11	0.19	1 sample t-test	**0.020**	22	0.81
		bias dPC ≠ 0 SST	0.06	0.30	1 sample t-test	0.450	14	
		bias dPC ≠ 0 CNO	0.17	0.28	1 sample t-test	0.051	12	0.74
		bias dPC ≠ 0 PRE	0.19	0.21	1 sample t-test	**0.010**	12	0.91
Figure 3	TABLE 1	Slope SST ≠ 0	-0.2	0.11	MWU-test	**0.002**	7	0.99
		Slope PV ≠ 0	-0.16	0.20	MWU-test	0.066	6	0.54
		Slope CB ≠ 0	0.13	0.39	MWU-test	0.370	6	0.12
Figure 5	TABLE 2	Slope HC L2 ≠ 0	0.39	0.66	MWU-test	0.379	6	0.3
		Slope HC L3 ≠ 0	0.13	0.34	MWU-test	0.379	6	0.16
		Slope HCO L2 ≠ 0	0.01	0.24	MWU-test	0.379	6	0.05
		Slope HCO L3 ≠ 0	-0.21	0.12	MWU-test	**0.005**	6	0.99
		Slope NEO L2 ≠ 0	-0.08	0.17	MWU-test	0.065	6	0.21
		Slope NEO L3 ≠ 0	-0.45	0.12	MWU-test	**0.005**	6	1

Supplemental Table 1: Summary stats for one sample t-test and Mann-Whitney U-test (MWU). M-mean, SD-standard deviation, SE- standard error, n- number of samples, “1-β” power analysis results at α: 0.05 given sample number**.** Bold: Significant p-values, red : 1-β < 0.7.

bioRxiv preprint doi: https://doi.org/10.1101/152975; this version posted July 31, 2017. The copyright holder for this preprint (which was not certified by peer review) is the author/funder, who has granted bioRxiv a license to display the preprint in perpetuity. It is made available under aCC-BY 4.0 International license.

Location		Regression	slope	r	Test	P	n	α: 0.05 1-β
Figure 1		Diff IPSC vs Diff Dist	5.8	0.57	F-test	**0.013**	19	0.7
		IPSC vs RC Dist	5.4	0.64	F-test	**0.003**	27	1
Figure 3	**Table 1**	SST-M1	-0.13	0.69	F-test	**0.001**	18	0.9
		SST -M6	-0.38	0.93	F-test	**0.000**	12	0.9
		SST -AVG	-0.25	0.94	F-test	**0.000**	10	0.9
		PV-M5	-0.44	0.75	F-test	**0.012**	10	0.75
		PV-Avg	-0.27	0.68	F-test	**0.030**	10	0.6
		CB-M3	0.67	0.68	F-test	**0.010**	13	0.75
		CB-M5	0.44	0.59	F-test	**0.021**	15	0.67
Figure 5	**Table 2**	HC L2-M4	1.62	0.78	F-test	**0.001**	14	0.9
		HC-L2 Avg	0.42	0.76	F-test	**0.016**	13	0.85
		HC L3	-0.34	0.65	F-test	**0.022**	12	0.65
		HCO-L2- M4	0.3	0.52	F-test	**0.037**	16	0.55
		HCO-L3-M1	-0.24	0.57	F-test	**0.033**	14	0.55
		HCO-L3-M6	-0.29	0.61	F-test	**0.012**	16	0.7
		HCO-L3-Avg	-0.19	0.76	F-test	**0.001**	16	0.9
		NEO-L2-M1	-0.32	0.54	F-test	**0.028**	15	0.55
		NEO-L2-M5	-0.1	0.79	F-test	**0.003**	11	0.85
		NEO-L3-M3	-0.34	0.79	F-test	**0.006**	10	0.8
Figure 5, 6, Table 2		NEO-L3-Avg	-0.47	0.97	F-test	**0.000**	14	0.95
Figure 6		IPSC vs RC Dist	0.67	0.97	F-test	**0.000**	27	1

Supplemental Table 2: Summary stats for F-test for non-zero slope of linear regression. n- number of samples, "1-β" power analysis results at α: 0.05 given sample number**.** Bold: Significant p-values, red : 1-β < 0.7. For density measures, power was analyzed for the mice yielding significant results but the lowest R-values and the lowest number of samples. These represent the minimum power for significant findings within the group.

bioRxiv preprint doi: https://doi.org/10.1101/152975; this version posted July 31, 2017. The copyright holder for this preprint (which was not certified by peer review) is the author/funder, who has granted bioRxiv a license to display the preprint in perpetuity. It is made available under aCC-BY 4.0 International license.

Location	Comparison	M 1	SD 1	n 1	M 2	SD 2	n 2	Test	P	α: 0.05 1-β
Figure 1 IPSC Strength	C vs R dPCs	4.18	3.92	19	2.6	2.96	19	paired t-test	**0.002**	0.8
	L2 vs L3 INT	3.42	2.12	18	7.02	4.60	25	ANOVA-Tukey	**0.004**	0.8
Figure 2 IPSC Strength	L3 dPC vs. INT	7.02	4.60	25	8.63	3.66	19	ANOVA-Tukey	n.s.	0.22
	R vs C sites INT	0.54	0.17	25	0.43	0.17	25	paired t-test	**0.008**	0.8
	C vs R sites PC	0.63	0.14	16	0.44	0.17	16	paired t-test	**0.003**	0.8
Figure 3 Density	PV < SST cells	109	22.05	6	235	37.04	7	Kruskal-Wallis	**0.005**	0.8
	PV < CB cells	109	22.05	6	174	66.14	6	Kruskal-Wallis	**0.005**	0.4
Figure 4 IPSC Strength	R vs C sites INT	0.58	0.14	22	0.479	0.15	22	paired t-test	**0.017**	0.75
	VGAT vs SST INT	6.82	6.57	22	7.02	4.60	25	unpaired t-test	0.910	0.05
	C vs R sites PC	0.51	0.12	15	0.57	0.12	15	paired t-test	0.500	0.05
	VGAT vs SST PC	4.77	3.21	13	8.63	3.66	19	unpaired t-test	**0.003**	0.91
	Pre vs CNO	4.14	2.42	12	2.72	1.39	12	paired t-test	**0.007**	0.8
	C vs R sites PC CNO	35	25.46	8	24	19.80	8	Wilcoxon	**<0.05**	0.8
Figure 5 Density	HC vs HCO L2	113	44.09	6	199	31.84	6	Kruskal-Wallis	**0.013**	0.9
	HC vs NEO L2	113	44.09	6	243	105.33	6	Kruskal-Wallis	**0.013**	0.6
	HC vs HCO L3	52	26.94	6	68	12.25	6	Kruskal-Wallis	0.149	0.19
	HC vs NEO L3	52	26.94	6	76	36.74	6	Kruskal-Wallis	0.149	0.21

Supplemental Table 3: Summary stats for two sample comparisons. M-mean, SD-standard deviation, n- number of samples, "1-β" power analysis results at α: 0.05 given sample number**.** Bold: Significant p-values, red : 1-β < 0.7. Abbreviations: C: Caudal, R: Rostral, INT: interneurons, PC: pyramidal cell, PV: parvalbumin, SST: somatostatin, CB: Calbindin, CNO: clozapine-n-oxide, HC: home cage no odor, HCO: Home cage plus odor, NEO: novel environment plus odor, L2: layer 2, L3: Layer 3. M: Mean, n: number of samples.